Final Report 2002-22

Research

The Impact of Roughness Elements on Reducing the Shear Stress Acting on Soil Particles

Minnesota Local
Road Research
Board

Technical Report Documentation Page

1. Report No. MN/RC – 2002-22	2.	3. Recipients Accession No.
4. Title and Subtitle THE IMPACT OF ROUGHNESS ELEMENTS ON REDUCING THE SHEAR STRESS ACTING ON SOIL PARTICLES		5. Report Date January 2002 6.
7. Author(s) Anita Thompson, Bruce Wilson		8. Performing Organization Report No.
9. Performing Organization Name and Address University of Minnesota Department of Biosystems and Agricultural Engineering 1390 Eckles Avenue St. Paul, Minnesota 55108		10. Project/Task/Work Unit No. 11. Contract (C) or Grant (G) No. c) 74708 wo) 168
12. Sponsoring Organization Name and Address Minnesota Department of Transportation 395 John Ireland Boulevard Mail Stop 330 St. Paul, Minnesota 55155		13. Type of Report and Period Covered Final Report 2001 14. Sponsoring Agency Code
15. Supplementary Notes		

16. Abstract (Limit: 200 words)

This report presents the results from a study on shear stress partitioning for vegetation. The project involved partitioning the shear stress from overland flow into one component that acts on the vegetation (form shear) and the remainder that acts on the intervening soil particles (particle shear). Particle shear is important for predicting soil erosion.

The study used idealized shapes to represent vegetal elements. Researchers designed and constructed a unique laboratory hydraulic flume, which they used in conjunction with hot-film anemometry to measure particle shear. They also designed and constructed instrumentation to measure the form shear on individual rigid vegetal elements, taking detailed spatial and temporal shear stress measurements for three element densities. Form shear was measured on each element within the test array. The study investigated a total of 16 test scenarios.

Particle shear accounted for 13 to 89 percent of the total shear. Shear partitioning theories developed for wind erosion adequately represent the observed data and can be used to determine an appropriate vegetation density for a threshold particle shear.

17. Document Analysis/Descriptors Vegetation Overland Flow Erosion	Shear Stress Partition Hot-Film Anemometry	18. Availability Statement No restrictions. Document available from: National Technical Information Services, Springfield, Virginia 22161	
19. Security Class (this report) Unclassified	20. Security Class (this page) Unclassified	21. No. of Pages 85	22. Price

THE IMPACT OF ROUGHNESS ELEMENTS ON REDUCING THE SHEAR STRESS ACTING ON SOIL PARTICLES

Final Report

Prepared by

Anita M. Thompson, PhD
Department of Biosystems and Agricultural Engineering
University of Minnesota

Bruce N. Wilson, PhD
Department of Biosystems and Agricultural Engineering
University of Minnesota

January 2002

Published by
Minnesota Department of Transportation
Office of Research Services
Mail Stop 330
395 John Ireland Blvd.
St. Paul, Minnesota 55155

Acknowledgements

The authors express appreciation to the Minnesota Local Road Research Board and the Minnesota Department of Transportation for support of this research and are indebted to Mr. Dick Larson, Mr. Leo Holm, and Mr. Dwayne Stenlund for their valuable assistance and support.

The authors would like to acknowledge several people whose work was instrumental to the completion of this study.

1. Brad Hansen, Brian Hetchler, and Todd Hustrulid; University of Minnesota, for the construction of experimental equipment.
2. Udai Singh, Verlyn Johnson, and Saby Sarkar; University of Minnesota, for their assistance with instrumentation and data collection.
3. Barb Oliver; University of Minnesota, for the editing of the manuscript.

Funding Acknowledgement

This project was conducted with the support of the Center for Transportation Studies (CTS). The CTS supports the research mission of the University of Minnesota with a broad program covering many topics related to transportation. The program includes both fundamental and applied research, with the goal of expanding the existing body of transportation knowledge.

This project was conducted with funding provided by the Minnesota Local Road Research Board (LRRB). The purpose of the LRRB is to develop and manage a program of research for county and municipal state-aid road improvements. Funding for LRRB research projects comes from a designated fund equivalent to one-half of one percent of the annual state aid for county and city roads. Substantial cost of the data acquisition system was provided by a companion project funded by the Minnesota Department of Transportation.

The fellowship for part of this study was provided by the United States Department of Agriculture National Needs Fellowship Program. Additional support was provided by the Minnesota Agricultural Experiment Station, Regional Project S-273.

TABLE OF CONTENTS

List of Figures

List of Tables

Executive Summary

Vegetation is widely used to stabilize earth (hill) slopes and protect against soil erosion. The interactions between vegetation and the processes responsible for particle detachment are not well understood, particularly, the relationship between the vegetation and the shear stress acting on soil particles. Vegetation partitions the total shear into one component acting on the large-scale roughness of the vegetation (form shear) and the remainder on the intervening soil particles (particle shear). Erosion is caused by soil particle detachment. The particle shear is responsible for particle detachment and, therefore, errors in determination of erosion can occur if total shear is used to predict particle detachment.

This study quantifies the shear partition (ratio of particle shear to total shear) for idealized vegetation. Instrumentation were designed and constructed to measure the components of the partition. A unique flume and hot-film anemometry were used to measure detailed spatial and temporal variations of particle shear. Instrumentation was developed to measure drag force on idealized shapes representative of vegetal elements.

For idealized vegetation, the shear partition is shown to decrease with increasing vegetative density. For the densities investigated, particle shear accounts for 13 to 89% of the total shear. Shear partitioning theories developed for wind erosin by Raupach (1992) and Wooding et al. (1973) are shown to adequately represent the observed data for water flows. The application of shear partitions to field design is possible using the theory of Raupach (1992). For example, the vegetation density (the ratio of plant upstream projected area to surface area) can be determined for a given threshold particle shear.

CHAPTER 1
INTRODUCTION

BACKGROUND

Soil is among humanity's most valuable natural resources. It is essential for adequate crop production, sustaining forested areas and plant communities, and plays an important role in the hydrologic cycle through infiltration and water storage. The problem of land degradation by soil erosion is worldwide with the primary driving force of either wind or water. In arid environments like the southwest United States where desert areas are sparsely covered by vegetation, wind is the primary erosive agent for soil detachment and transport (Wolfe and Nickling, 1996). In addition to land degradation in these areas, wind produces dust, which can be detrimental to the health of humans as well as animals. Water, in the form of raindrop splash, sheet flow, streamflow, rill, and gully flow is the driving erosive force in other areas (Foster, 1982). In the United States approximately three-fifths of estimated erosion is due to water moving over the soil surface (Gray and Sotir, 1996).

Total erosion in the United States was estimated at 6.91 billion tons (3.6 tons/acre) in 1992 (Magleby et al., 1996). Economic losses from erosion are both direct, including property damage from sediment accretion or loss, and indirect, including flooding, drainage disruption, and gullying (Gray and Sotir, 1996). Loss of fertile topsoil reduces crop productivity and increases the need for fertilization. Transported sediment and adsorbed polluting chemicals and nutrients degrade water quality of lakes, streams, rivers, oceans, and reservoirs (Foster, 1982). Migration of streams and rivers as a result of streambank and gully erosion leads to a reduction in usable land. Clear-cutting in forested areas, particularly in mountainous areas with steep slopes, weakens soils and destabilizes slopes which can result in mass erosion from debris slides. Approximately one-fourth to one-third of the total amount of eroded sediment reaches the oceans (Gray and Sotir, 1996). The remainder is deposited in streams, lakes, and reservoirs. In the United State's waterways, eroded sediment is the number one pollutant in terms of both quantity and adverse effects (Gray and Sotir, 1996).

Significant research has been done to study erosion from agricultural areas. Soil erosion as a result of urbanization is a major source of sediment and non-point source pollutants. Soil erosion from a construction site without proper soil erosion and sediment control practices can average 20 to 200 tons/acre/year, which is 10 to 20 times greater than typical soil loss on agricultural lands (USDA, 1999). Establishment of vegetation is a widely used soil erosion practice at construction sites. Little information is available on the interactions between vegetation and processes responsible for particle detachment.

The soil erosion process consists of three components: detachment, transport, and deposition of soil particles. Detachment of soil by water is via raindrop impact or via the shear force of flowing water exerted on soil particles. Sediment is transported down slope primarily by flowing water and minimally by raindrop splash (Haan et al., 1994). As wind or water moves across a surface, it exerts a shear force on the surface. Figure 1.1 is a schematic of the forces acting on a soil particle. The drag (F_d) and lift (F_L) forces are opposed by the resistive forces which include the weight of the particle (W_S) and the cohesive/contact forces with adjacent soil particles (F_{C1} and F_{C2}). The point at which the moment resulting from the drag and lift forces equals the moment resulting from the resistive forces, is referred to as the point of incipient motion (Lavelle and Mofjeld, 1987). Particle detachment occurs when the drag force on a soil particle overcomes the resistive forces of the particle **(**Wilson, 1993; Gray and Sotir, 1996**)**.

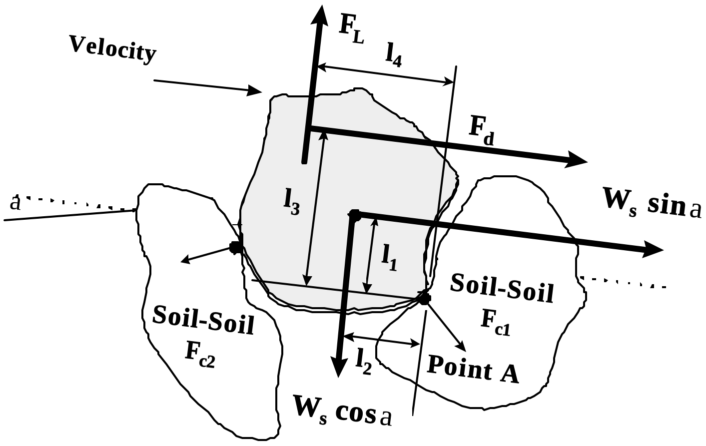

Figure 1.1. Forces Acting on a Soil Particle (Wilson, 1993a).

Vegetation increases hydraulic resistance to flow, thereby increasing flow depths and reducing flow velocities. For wind erosion vegetation plays a stabilizing role by covering the soil surface, trapping soil particles, and extracting momentum from the air (Wolfe and Nickling, 1993). Similarly, for water, vegetation protects the soil surface from raindrop impact, retards flow, and enhances deposition (Foster, 1982). Vegetation stabilizes hillslopes by reinforcement of the soil matrix through the root structure. Vegetation also reduces the shear stress on the soil surface (Wyatt and Nickling, 1997). Ultimately, vegetation influences the soil erosion process by altering the shear applied to the soil particles and changing soil erodibility. Figure 1.2 shows sparse vegetal stems in a partially eroded roadside ditch and understanding the role of vegetation is necessary to properly design the channel.

Vegetation partitions the shear force from overland flow into one component acting on the vegetation (form shear) and the remainder on the intervening soil particles (particle shear). Particle shear is responsible for detachment in the erosion process. The ratio of particle shear to total shear is commonly referred to as the shear stress partition. Currently, little information is available on the fraction of the total shear that acts on the soil surface when vegetation is used to control erosion. The relationship among vegetation, overland flow and the fundamental processes influencing soil erosion is not well understood. It is important to understand these interactions to gain insight into the erosion process and to improve prediction accuracy. In addition, errors can be expected if the total shear is used to predict potential soil erosion.

Figure 1.2. Partially Eroded Highway Roadside Ditch with Sparse Vegetation.

An intuitively appealing approach for this study is to use naturally occurring vegetal elements. The geometric form of natural vegetation is, however, complex and highly variable. This complexity makes it difficult to design an experiment to isolate the physical characteristics of plants that are important in determining drag force. Furthermore, inherent variability among and within plant species requires a large number of tests to quantify the results. Because of these limitations, this study will use idealized shapes to represent the physical characteristics of vegetation.

Extensions to natural vegetation are likely from reliable drag force measurements obtained from the idealized shapes. For example, assume that upstream projected surface area with depth is an important physical characteristic influencing the drag coefficient. Application of the drag force results to natural vegetation would simply require the determination of the surface-area-depth relationship for the plant of interest. These relationships and parameters are much easier to obtain than measuring drag force directly for individual plants in the flume. Complexities associated with leaf and stem spatial distribution can conceptually be tied to variability in the surface area-depth relationship, avoiding time-consuming measurements. This second-step hypothesis needs to be evaluated with a systematic set of experiments and needs only to be undertaken if the first step is successful.

OVERVIEW OF RELATED WORK

Hydraulic Resistance

Large-scale roughness in the form of micro-relief, soil particles and aggregates, or vegetation increases resistance to flow, reduces flow velocity and increases flow depth. Common relationships used to determine flow capacity or velocity as a function of the resistance to flow in conduits are the Chezy, Darcy-Weisbach, and Manning equations (Streeter and Wiley, 1985). Each contains empirical roughness coefficients. Values for roughness coefficients are well established for a number of different materials (i.e., concrete, steel) but are not as easily applied to vegetation.

Vegetation is used in the design of waterways to stabilize channels and reduce erosion. The use of a single roughness coefficient (n) to describe resistance to flow for vegetation poses two problems. The first is that different types of vegetation provide different resistance to flow (Kouwen and Li, 1980), and second, the resistance changes as the depth of flow changes (Palmer, 1945). The relationship between roughness coefficient and depth of flow is highly variable and nonlinear for vegetated channels (Palmer, 1945). Flow through vegetative waterways is generally characterized by three regimes (Palmer, 1945; Temple, 1982, Kouwen and Unny, 1973). The regimes are low flows that do not bend or submerge the plants or stems, intermediate flows that bend and submerge the vegetation, and high flows that result in the vegetation deflecting in the direction of flow. Therefore, the roughness provided by the vegetation is a function of flow depth. Methods that account for the effects of the bending of vegetation on resistance to flow are given by Palmer (1945), Kouwen and Li (1980), Temple (1982), Thompson and Roberson (1976), and Chen (1976).

Another relationship commonly used to describe resistance to flow is the friction factor versus Reynolds number (f-Re). This is well established for pipe flow as described by the Moody diagram (Streeter and Wylie, 1985) and similar relationships exist for shallow flow over a smooth or rough plane bed surface (Abrahams et al., 1986). Abrahams and Parsons (1991) provide a regression equation for predicting f from Re, percent gravel, and a measure of roughness.

Chen (1976) studied resistance to shallow flow over natural turf surfaces using both Kentucky Blue Grass and Bermuda Grass. Chen found the friction factor decreased with Reynolds number in the laminar flow range. Using flexible plastic strips, Kouwan and Unny (1973) studied the effect of roughness in a laboratory flume. For the erect and waving positions, the friction factor was primarily a function of relative roughness. For the prone position, friction factor was a function of Reynold's number. They also found the friction factor was reduced by more than a factor of five when the strips became prone.

In addition to increasing hydraulic roughness, large-scale surface roughness affects sediment yield. Using fiberglass electrical sleeving to simulate straw mulch, Kramer and Meyer (1969) found rill development decreased as mulch increased. Kramer and Meyer found mulch rates of 0.5 to 1 ton/acre greatly reduced erosion rate and runoff velocity compared to no mulch. Benik et al. (1999) examined the impact of blankets on controlling erosion and vegetative growth for a construction site. They found straw mulch reduced erosion by about a factor of 10 compared to bare soil plots for a simulated rainfall event. The use of erosion control blankets is shown to significantly reduce soil loss when compared to bare soil plots by Gharabaghi et al. (2000a). Li and Shen (1973) found staggered patterns of tall vegetation (as opposed to parallel patterns) were most effective at reducing flow rates and sediment yields from watersheds.

Vegetative filter strips (VFS) provide localized erosion control and treat nonpoint source pollution by providing an opportunity to filter sediment, nutrients, and other pollutants from runoff (Dillaha et al., 1989). VFS reduce sediment loads by retarding the flow velocity and decreasing the transport capacity of flow (Tollner et al., 1982). Through field experiments, Gharabaghi et el. (2000b) show that sediment removal efficiency of VFS is between 80 and 95%. Gharabaghi et al. (2000b) also discusses that addition of a geosynthetic can improve the runoff treatment performance of VFS.

Although these studies provide useful information on hydraulic roughness and sediment yield for vegetated conditions and erosion control blankets, they do not give information on the interactions between large-scale surface roughness, overland flow, and the resulting shear force applied to the soil surface. Soil erosion is the result of surface drag forces overcoming the resistive forces acting on soil particles (Wilson, 1993). The forces resisting motion for coarse sediment are mainly due to the weight of the particles while cohesion is the main resistive force for fine sediments (Task Committee, 1966). As shown by Lane and Nearing (1989), shear stress is critical for predicting soil erosion. In a laboratory study, Ghebreiyessu et al. (1994) found detachment increased with increasing shear stress. In a lab study, Govers (1990) found a primarily linear relationship between solid discharge and shear stress. A sharp rise in the volumetric sediment concentration was observed at a shear velocity of approximately 3 cm/s that implies a threshold for rill erosion (Govers, 1990).

Movement of water across a rough surface generates a resistive force on the surface. A fraction of the total resistive force acts on the roughness (form shear) and the remainder acts on the intervening soil surface (particle shear). Vegetation increases the total resistive force while decreasing the fraction of the total acting on the soil surface. The ratio of particle shear to total shear is generally referred to as shear stress partitioning.

Shear Stress Partitioning

A sheet of sand paper is used by Einstein and Banks (1950) to illustrate the concept of shear partitioning:

> *If this sand paper is laid flat on a flat bottom it gives a roughness according to its grain. This same sand paper, on the other hand, may be arranged in the shape of a corrugated sheet. In this case the corrugation and the grain represent two different types of roughness which are superimposed over one another.*

Schlichting (1936) first proposed that the total drag force (F) applied to a rough surface be divided into that exerted on the roughness elements (form drag, F_R) and that on the intervening surface (particle drag, F_S):

$$F = F_R + F_S \tag{1.1}$$

Dividing by the ground area (A), leads to the basic shear stress partition equation:

$$t = \frac{F_R}{A} + t_S \frac{A'}{A} \tag{1.2}$$

where τ and τ_S are the total shear stress and the shear stress exerted on the surface, respectively, and A' is the ground area not occupied by roughness elements.

The pioneering laboratory study of Einstein and Banks (1950) used combinations of blocks with and without pegs, and with and without offsets to model vegetation and sandbars. Einstein and Banks postulated that the total resistance was the superposition or sum of the individual resistance of the vegetation, the sand bars, and the particles composing the river bed.

The shear partition has been investigated for alluvial streams where total hydraulic roughness is from grain roughness and form roughness (van Rijn, 1984; Griffiths, 1989; Li, 1994). Here, high discharges cause a flattening of the stream bed and antidune formation, while low discharges result in the formation of ripples and dunes. The bed configuration impacts the flow resistance which in turn affects the discharge. One of the central problems of flow resistance in mobile channels is an estimation of the roughness coefficient. Due to the dynamics of this system, stage-discharge relationships are highly variable and estimation of form resistance is very difficult. Depth-discharge relationships are important in calculating sediment transport rates, flow routing, channel stability, and waterway design (Griffiths, 1989).

Alam and Kennedy (1969), considering sand bed channels, and Griffiths (1989), considering gravel bed channels, divided the energy slope into form and particle components. Einstein and Banks (1950) and Engelund (1966) suggested a similar division of the total hydraulic radius for alluvial streams. The sediment transport capacity in alluvial streams is controlled by the grain shear stress (Li, 1994). This fact is important because the grain shear stress can be considerably smaller than the total shear stress resulting in errors in predicting sediment transport if the total stress is used.

Concepts identified for alluvial streams are also applicable to hillslope runoff. Govers and Rauws (1986) examined data from two individual experimental setups. On a plane bed they observed a clear relationship between total shear velocity of flow and transported sediment concentration. However, no good correlation was apparent for an irregular bed. This led to the hypothesis that sediment transport is not a function of total shear but rather only of particle shear. Foster et al. (1982) divided the total shear stress into grain and form components when studying the hydraulics of mulch failure for determining critical slopes for erosion control.

Dividing the depth of flow into the form and grain components Prosser et al. (1995) found cumulative sediment yield was shown to lie on a single curve when plotted against grain shear. On undisturbed plots, mean boundary shear stresses of at least 1000 to 1800 dynes/cm^2 were required to transport sediment. After complete removal of plant stems, the shear stress required to transport sediment was 11 to 38% of that required on the undisturbed plots. Prosser et al. (1995) show that on a densely grassed surface over 90% of flow resistance is exerted on plant stems using the concept of shear stress partitioning.

Rauws (1988) calculated the grain and form friction factors from measured hydraulic parameters to investigate flow friction due to composite roughness. Govers (1987) uses Savat's (1980) algorithm to determine the bed friction factor, from unit discharge and depth, which was then used to determine the bed shear stress. Abrahams and Parsons (1991) explain that large errors can be expected when using the total shear as opposed to the grain shear in sediment transport formulas because form roughness plays a significant role.

A theoretical framework for evaluating the shear partition is important for erosion prediction for a variety of vegetated conditions. Raupach (1992) proposed a theoretical framework for predicting the shear partition. Raupach's theory is a geometrical approach that uses representative areas and volumes to account for the reduction in surface shear stress and drag force as a result of roughness elements. The predictive equation is

$$\frac{t_S}{t} = \frac{1}{1 + b\,l} \tag{1.3}$$

where τ_S is the particle shear, τ is the total shear, β is the ratio of element drag to surface drag, and λ is the roughness density. Raupach et al. (1993) analyzed the effect of roughness density (ratio of frontal area to ground surface) on the threshold friction velocity ratio. They were able to adequately describe the ratio in terms of the roughness density parameter and the basal/frontal area ratio of the element. Additional theoretical work on partitioning includes evaluation of the movement of arctic pack ice (Arya, 1975), the dynamics of mobile sand ripples (Li, 1994), and processes of wind erosion (Wooding et al., 1973).

Although the theory of Raupach (1992) was developed for wind erosion, the theory should be applicable to water with modifications. As given by Equation 1.3, the theory is dependent on the geometric characteristics of the vegetation and the drag coefficient for individual vegetal elements. Previous work on evaluating the shear partition has focused in two main areas. As previously discussed, the first, for water, is the division of energy slope or hydraulic radius into that corresponding to form shear and that corresponding to particle shear. For wind, it includes both field and laboratory studies in which both components have been measured.

Marshall (1971) investigated variations of roughness element density, size, shape, form, horizontal distribution, and orientation in a wind tunnel to evaluate the role of vegetation in reducing wind erosion on agricultural fields. Here the total drag force on the surface was determined with the momentum integral and by measurement (replaced part of floor with balance) and the drag on individual elements was also measured. Marshall found that an area of ground does not have to have complete cover for the average surface shear stress to be negligible. Marshall determined that at an element spacing ratio (diameter/height, d/h) of 5 to 6 and that d/h ratios between 1 and 3 are common to many woody perennial plants. Marshall also found that arrays of randomly distributed elements exert less drag than the equivalent arrays of regularly distributed elements. However, this difference is small.

Lower vegetation density results in a lowering of the threshold friction velocity which is the friction velocity required to initiate motion of soil particles (Stockton and Gillette, 1990). To determine the sheltering effect of vegetation on soil erodibility, Stockton and Gillette (1990) followed up on Marshall's (1971) analysis on shear stress partitioning by using the ratio of threshold friction velocity for bare soil to that for vegetated soil. The threshold friction velocity for bare soil was measured in a wind tunnel by increasing wind speed until continuous movement of soil particles was first visible. Wind profile measurements were made and fitted to the log-velocity profile. Threshold friction velocity for vegetated sites were made in the field by measuring the velocity profile and a 'Sensit' erodible mass monitor which detects impacting particles. Wolfe and Nickling (1996) also investigated a shear velocity ratios.

Wyatt and Nickling (1997) evaluated Raupach et al. (1993) shear stress partitioning theory in the field. The total shear stress was determined by measuring the wind profile upwind of the vegetation and surface shear was measured using an Irwin sensor which is a type of skin friction meter. The authors found the model of Raupach et al. (1993) to accurately represent the shear velocity ratio over surfaces of varying roughness concentrations. Wyatt and Nickling (1997) were able to simultaneously measure the total shear stress and surface shear stress in the field.

Investigation of the shear partition requires measurement of individual drag components. To date, attempts to measure the individual components have, in general, been for wind erosion where the element is totally immersed in the wind profile. A significant difference for water erosion is that the roughness elements can be partially or completely submerged.

Measurement of Form and Particle Shear

As shown by the previously mentioned wind studies and given by Equation 1.1, accurate evaluation of the shear partition involves measurement of two of the three components. More specifically, the drag on large-scale roughness elements and/or the drag on the intervening soil particles, and/or total shear directly.

The measurement of drag forces on vegetation in overland flow is complicated by the effects of the boundaries (fixed and free) and also the variations in plant frontal area with depth of flow. Few studies exist that account for these variations over a range of flow conditions. Petryk (1969) measured drag forces on cylinders in open channel flow over a range of diameters and depths using a drag balance. Drag coefficient was found to be a function of Froude Number based on depth of flow and diameter of cylinder. Bokaian and Geoola (1984) studied wake interference for two circular cylinders at various orientations to each other. Theoretical approaches to drag on vegetation are presented by Petryk and Bosmijian (1975), Jadhav and Buchberger (1995), and Li and Shen (1973).

Downwind of a roughness element, a wake develops within which the velocity of the flow is reduced. Accelerated flow occurs on the sides of the element as air is forced around the element. An area of decelerated flow exists behind the element (Wolfe and Nickling, 1993). With increase in element density, the surface area protected by the reduced flow velocities increases.

Using a formulation for the spread and decay of a circular cylinder, Li and Shen (1973) determined the effects of cylinder spacings and patterns on mean drag coefficients. The addition of cylinders causes increased interactions with the wakes of other cylinders and therefore the drag coefficient does not remain the same for all cylinders.

Using rigid metal pegs as vegetal media, Tollner et al. (1976) studied sediment filtration capacity of vegetation for a range of element spacings. The use of well-defined objects allows accurate accountability of geometric characteristics. Experiments can then effectively study the impacts of these characteristics on flow properties. Rigid cylinders have been used to represent vegetation (Jadhav and Buchberger, 1995; Lopez et al., 1995; Li and Shen, 1973; Nepf et al., 1999; and Tollner et al., 1982). Uniform rectangular plastic strips have been used by Kouwen and Li (1980), Kouwen and Unny (1973) and Kao and Barfield (1978).

The velocity profile for steady turbulent flow near a flat surface is described by the "law of the wall"

$$\frac{u}{u_*} = \frac{1}{k} \ln \frac{y}{y'} \tag{1.4}$$

where u is the velocity at a distance y from the surface; u_* is the shear velocity at the wall defined as $\sqrt{t_S / r}$,where t_s is the shear stress at the surface and ρ is the density of water; κ is von Karman's constant; and y' is the distance such that $u = 0$ at $y = y'$ (Garde and Ranga Raju, 1985). This equation is used to describe both wind and water flow. Kouwan and Unny (1973) found the log-velocity profile to suit the conditions of flow through artificial plastic strips and observed a layer of almost constant low velocity within the grass near the bed. This low velocity was proportional to the overall shear velocity. Prosser et al. (1995) also observed a layer of slow flow at the boundary that scales with the size of the roughness elements. However, Prosser et al. (1995) explain that large roughness elements have been shown to limit the development of the log-velocity profile.

The average shear stress in a steady uniform flow in a wide open channel is determined by measuring the depth of flow and the slope of the water surface and is determined as (Garde and Ranga Raju, 1985)

$$t_0 = gRS \tag{1.5}$$

Variables have been previously defined. However, uniform flow does not exist when vegetation is present, therefore another method is needed. Other instrumentation developed for direct measurement of bed shear stress are discussed by Vakili (1986), Tanner (1979), Preston (1945), and Reda et al. (1994).

Hot-wire or hot-film anemometry (HWA, HFA) is based on the principles of convective heat transfer from a heated sensing element. The heat transfer from the film in fluid flow is dependent on both the properties of the fluid (density, viscosity, thermal conductivity, specific heat) and the parameters of the flow (velocity, temperature, pressure) (Bruun, 1995). As the fluid flows past the sensor, the rate of cooling of the sensor is related to the velocity of the flow over it. A constant temperature thermal anemometer supplies additional voltage to the sensor to maintain it at a constant temperature.

Hot-film sensors can be mounted flush with an inside wall to minimize flow disturbance. Hot-film sensors are a thin layer of platinum or nickel, deposited on a thermally insulated substrate. This substrate is usually quartz. Calibration should be carried out under well-defined experimental conditions. Examples of measurements of surface shear stress in water flows using hot- film anemometry are given by Li (1994), Garcia et al. (1998), and Robinson (1989).

OBJECTIVES

The overall goal of this research is to quantify the fraction of the total shear, resulting from overland flow, that acts on the soil particles in the presence of vegetation. This is accomplished through the following objectives:

1) To develop methodology and instrumentation for measuring particle shear for channel flows with and without vegetal elements;
2) To develop methodology and instrumentation for measuring form shear of idealized vegetal elements and for determining their drag coefficients;
3) To determine shear partitioning for idealized vegetal elements using measured particle shear and element drag forces;
4) To modify and evaluate existing shear partitioning theory for flow with vegetal elements.

ORGANIZATION OF REPORT

This report consists of two main chapters each containing an overview of activities, experimental equipment and procedures, results, and summaries. Chapter 2 details the instrumentation and methodology used to measure form shear on idealized vegetal elements. Chapter 3 details the instrumentation and methodology used to evaluate the shear partition for idealized vegetation. Chapter 4 is an overall summary and the conclusions of our research.

CHAPTER 2

FORM DRAG ON IDEALIZED VEGETAL ELEMENTS IN OVERLAND FLOW

INTRODUCTION

Information on the drag of vegetative elements is necessary to understand the effects of vegetation on partitioning the total shear into particle and form components. Estimating the drag force for vegetation under a range of flow conditions is important in assessing the vegetation density and height required for erosion control prediction under different flow conditions. This chapter details the instrumentation designed and constructed to measure drag forces on rigid elements representative of vegetation in overland flow. Results are presented in terms of drag force and dimensionless drag coefficients.

INSTRUMENTATION

Laboratory Flume

Figure 2.1 shows a picture of the hydraulic flume used to carry out the experiments. Water is supplied to the flume inlet tank by two parallel pipes (7.62 cm pipe diameter for low flows and 15.24 cm pipe diameter for high flows) connected to a pump and 2.84 m^3 reservoir. The rate of discharge is controlled by valves and is measured by calibrated orifice plates connected to differential manometers. The total length of the flume is 7.32 m and consists of a 3.66 m development section followed by a 0.61 m test section and a 3.05 m outlet section. The width of the flume is 0.38 m and the height of the sidewalls is 0.38 m. The slope of the flume is adjustable via screw jacks positioned lengthwise along the flume. Velocity measurements were made along a transect in the test section using a static-pitot tube to determine the velocity region of the flume influenced by the sidewalls. These measurements show that flow velocities are uniform for all measured points. The first and last values are 7.6 cm from either sidewall.

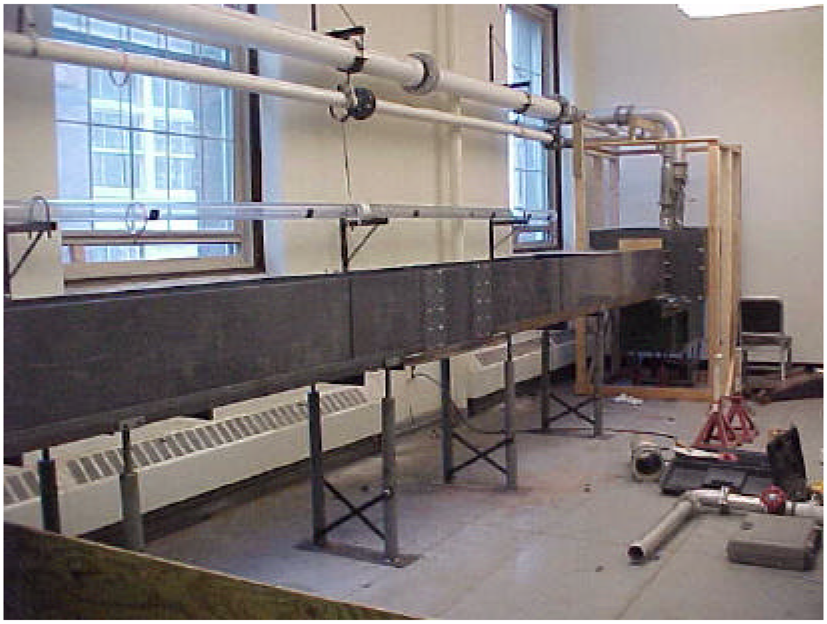

Figure 2.1. Laboratory Flume.

Drag Force Instrumentation

The drag force on vegetal elements is investigated using a unique instrumentation system developed for this project. The device consists of a load cell (oriented such that the load is applied in the horizontal direction) connected to a low friction linear slide. A threaded rod is rigidly connected to the slide and the cylinder is threaded onto the free end of the rod. As shown in Figure 2.2, the load cell and slide are rigidly connected to a support structure that is mounted to the top of the flume. The object is positioned such that a small space exists between the bottom of the object and the floor of the flume. This is to eliminate friction forces between the object and the flume floor. Flow under the element is very small and therefore its contribution to the total drag force is neglected.

Drag force causes linear movement in the slide. This movement is a tensile force for the load cell and is measured as voltage. A Strawberry Tree data acquisition system (Strawberry Tree, Inc., 1993) and Macintosh 7100/80AV computer convert the voltages to forces using a calibration curve. Although the slide assures linear motion, frictional forces exist within the slide and are likely complex. To avoid possible errors caused by frictional forces, the load cell readings are calibrated for the conditions of this study. The details are described in the following section.

EXPERIMENTAL PROCEDURE

An initial set of drag force measurements were made with a horizontal flume. These preliminary measurements are not the main focus of the study, but are nonetheless still useful and will be presented. Greater interest lies with the measurements gathered with the flume at a 1% slope. The 1% slope corresponds to the experimental conditions for measuring the shear partition in Chapter 3. The drag force instrumentation was calibrated at each slope prior to running the experiments. A schematic of the drag force instrumentation is shown in Figure 2.2. The calibration procedure is described below.

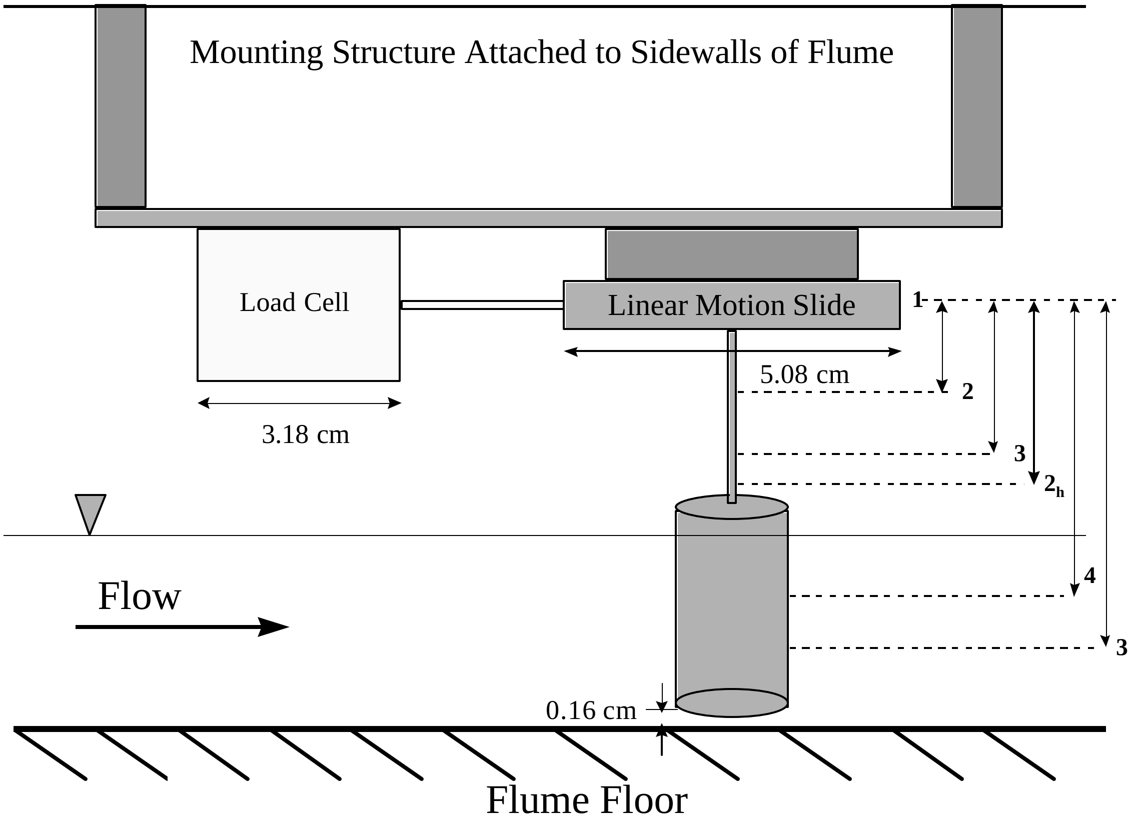

Figure 2.2. Drag Force Instrumentation (not to scale). Calibration Locations are 1-4, 2_h, and 3_h. Distances are 1-2) 3.8 cm; 1-3) 7.8 cm; 1-4) 13.7 cm; 1-2_h) 8.9 cm; 1-3_h) 14.6 cm.

Calibration of Drag Force Instrumentation

The drag force instrumentation was calibrated by applying a range of known forces with a spring balance. Separate calibrations were performed for the horizontal and 1% flume slope. The forces were applied at locations 1, 2_h and 3_h for the horizontal flume and at locations 1, 2, 3, and 4 for the 1% flume slope. The locations are shown in Figure 2.2. The spring was supported by a small jack stand that could be manually adjusted to assure that the force was in line with the load cell. The other end of the balance was attached to a vice. The vice assured that the force was held constant. The voltage from the load cell was recorded at 20 Hz for 2 minutes. A consistent reading was obtained for each load. The coefficient of variation defined as

$$C_V = \frac{S_X}{\overline{X}} \tag{2.1}$$

where $\overline{X}$ is the average voltage and S_X is the standard deviation of the voltage, was typically 0.002. This low value indicates the stability of the voltage reading. An average voltage for each force was calculated. A linear relationship between voltage and force was developed as

$$V = mF + b \tag{2.2}$$

where V is the measured voltage, F (N) is the applied horizontal force, m and b are the slope and intercept, respectively. The calibration was performed at different locations to evaluate the impact of the location of the resultant force. The regression slopes are fortunately similar for all locations. Because the velocity distribution is non-uniform, determining the location of the resultant drag force is difficult, requiring a detailed velocity distribution. It is therefore desirable to use a single calibration rather than a different equation dependent on location. At each flume slope, the average calibration from all height locations is used to determine drag forces. The calibration data and regression equations are shown in Figure 2.3.

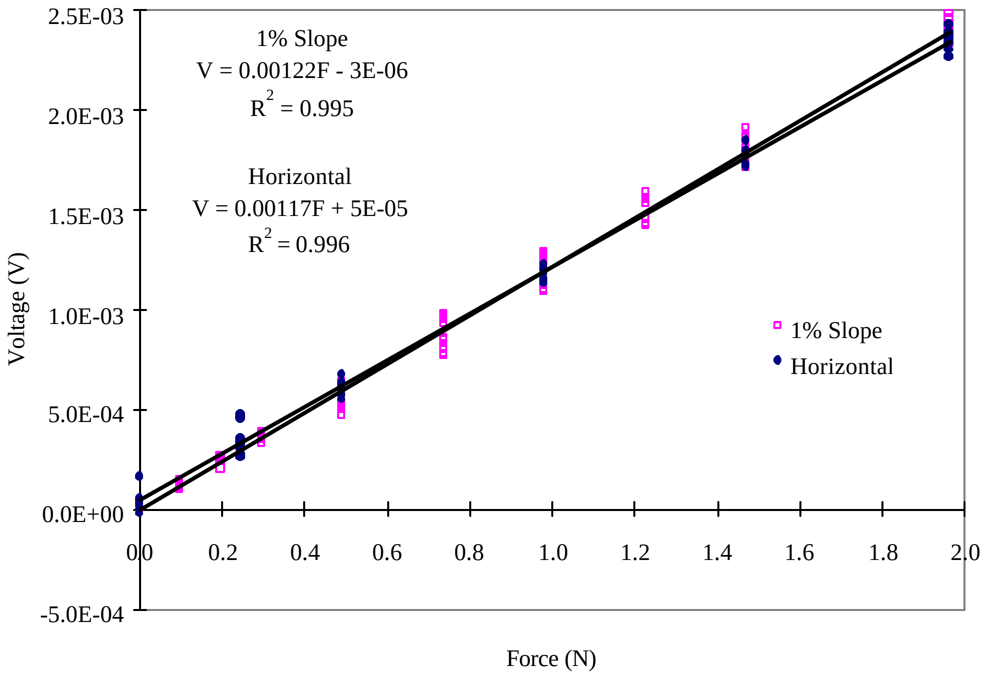

Figure 2.3. Drag Instrumentation Calibrations.

An error analysis to determine the magnitude of the error in the drag coefficient using an average regression slope is presented in the Results Section. Approximately 6 months was between calibrations of the horizontal and 1% slopes. During this time the instrumentation was not used. This likely accounts for the shift in calibration constants.

Idealized Shapes of Roughness Elements

Four idealized shapes were investigated: cylindrical (C), rectangular (R), trapezoidal with large base oriented at the flume floor (TL), and trapezoidal with small base oriented at the flume floor (TS). The shapes and their dimensions are shown in Figure 2.4. The cylinders were constructed from PVC rod and the remaining shapes from solid PVC, 0.95 cm thick. In addition to modeling plant stems, the cylinders were used to compare the measured drag forces to previously reported values. The trapezoids account for decreases and increases in upstream frontal area with depth of flow. The widths of the cylinder and rectangle are 2.54 cm and the bases of the trapezoids are 4.13 cm and 0.95 cm.

For each element shape, four heights were investigated: 2.54 cm, 5.08 cm, 7.62 cm, and 10.16 cm, resulting in a total of 16 elements. The elements were designed to ensure that at submergence, elements of the same height have equal upstream wetted area. Only the 7.62 cm height elements were investigated for the horizontal flume.

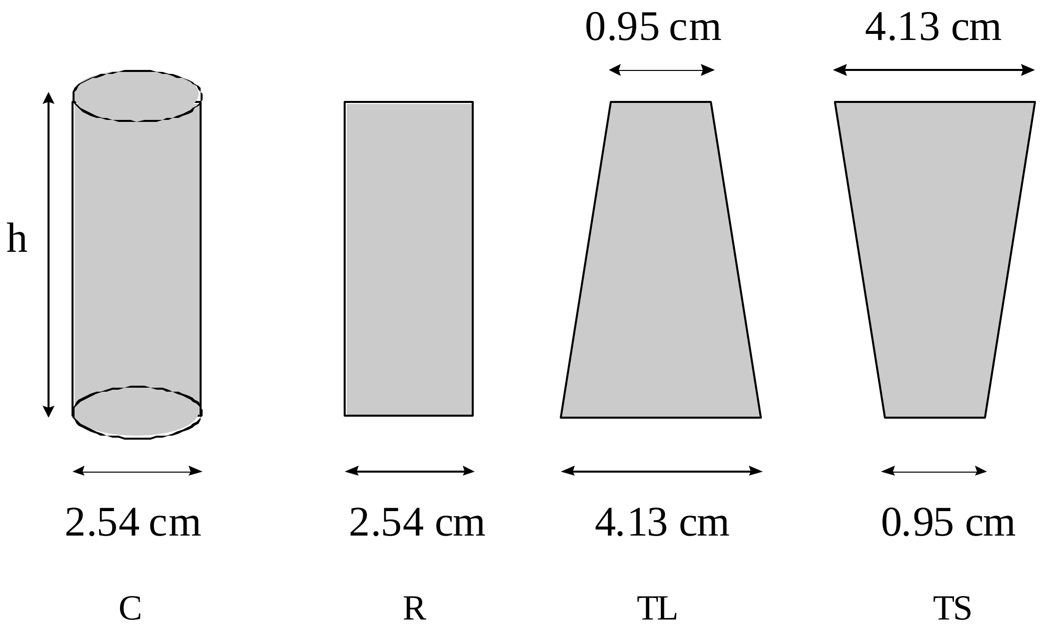

Figure 2.4. Idealized Shapes (not to scale), h = 2.54, 5.08, 7.62, and 10.16 cm.

Measurements of Drag Force

The slope of the flume was first set. The distance from the linear slide to the bottom of the element was held constant. For the experiments, it was important to have the bottom of the element as close to the bottom of the flume as possible without touching the flume to more accurately represent the connection between plants and ground. By not touching the flume, any frictional forces between the element and the floor could be neglected. A screw jack mounted on the top of the flat plate allowed for adjusting the height of the measurement system. A metal plate (0.16 cm) was placed on the floor of the flume and the element position adjusted so that it just rested on the plate. The plate was removed leaving a small space between the element and the flume. A zero reading was first obtained by recording the voltage from the load for no applied force. The pump was then turned on and water was allowed to recirculate through the flume. Once steady state conditions were reached (as measured by a constant flow depth), the flow rate was recorded, the upstream flow depth was measured, and the force on the element was measured by recording the voltage from the load cell. The flow rate was increased and the procedure repeated. Four flow conditions were investigated, resulting in a combination of partial and complete submergence of the elements. Tables 2.1 and 2.2 show the average flow rate, flow depth, and velocity (obtained by dividing the flow rate by the cross sectional area) for the four experimental conditions for the horizontal and 1% flume slopes, respectively.

Table 2.1. Experimental Flow Conditions (Horizontal).

Flow Condition	Average Flow Rate ($m^3 \cdot s^{-1}$)	Average Flow Depth (cm)	Average Velocity ($m \cdot s^{-1}$)
I	0.005	2.84	0.41
II	0.008	4.47	0.48
III	0.019	7.49	0.66
IV	0.028	9.75	0.75

Table 2.2. Experimental Flow Conditions (1% Flume Slope).

Flow Condition	Average Flow Rate ($m^3 \cdot s^{-1}$)	Average Flow Depth (cm)	Average Velocity ($m \cdot s^{-1}$)
I	0.004	1.93	0.59
II	0.008	2.83	0.74
III	0.010	3.32	0.81
IV	0.020	5.06	1.02

Uncertainty in Drag Coefficient

Uncertainty in the calculated drag coefficient is determined using the methodology described by Beckwith et al. (1982). For a given function, Taylor's theorem can be expressed as

$$\begin{aligned} & f\left[(x_1+\Delta x_1),(x_2+\Delta x_2),\cdots(x_n+\Delta x_n)\right]= \\ & f(x_1,x_2,\cdots x_n)+\Delta x_1\frac{df}{dx_1}+\Delta x_2\frac{df}{dx_2}+\cdots\Delta x_n\frac{df}{dx_n}+higher\_order\_terms \end{aligned} \quad (2.3)$$

where the x_n's are variables and the Δx_n's are uncertainties in the respective x_n's. By neglecting the higher order terms and rewriting terms, the uncertainty associated with measurement errors is defined as

$$\begin{aligned} & f\left(\left|x_1\right|+\left|u_{x_1}\right|\right),\left(\left|x_2\right|+\left|u_{x_2}\right|\right),\cdots\left(\left|x_n\right|+\left|u_{x_n}\right|\right)-f\left(\left|x_1\right|,\left|x_2\right|,\cdots\left|x_n\right|\right)=u_f \\ & =\left|u_{x_1}\frac{df}{dx_1}\right|+\left|u_{x_2}\frac{df}{dx_2}\right|+\cdots+\left|u_{x_n}\frac{df}{dx_n}\right| \end{aligned} \tag{2.4}$$

where u_f is the overall maximum uncertainty in the function. A more reasonable estimate of uncertainty corresponds to the Pythagorean summation of the discrete uncertainties (Beckwith et al., 1982), or

$$u_f=\sqrt{\left(u_{x_1}\frac{df}{dx_1}\right)^2+\left(u_{x_2}\frac{df}{dx_2}\right)^2+\cdots+\left(u_{x_n}\frac{df}{dx_n}\right)^2} \tag{2.5}$$

RESULTS AND DISCUSSION

Drag measurements are presented as actual drag forces and as drag coefficients. The drag force is a function of upstream projected area and flow velocity. Drag coefficient is a dimensionless representation of the drag force and corresponding flow parameters.

Drag Force

Drag force is a function of upstream projected area and velocity. In general, drag force increases with upstream projected area and flow velocity. Standard fluid mechanics relationships predict a direct linear relationship between drag force and projected wetted area (for the same velocity squared) (Streeter and Wylie, 1985). A linear regression of the following form was fitted to the data

$$\frac{F}{U^2}=mA+b \tag{2.6}$$

where F (N) is the drag force, A (m^2) is the upstream projected area, and m and b are regression parameters. Figure 2.5 shows the relationship described by Equation 2.6 and the corresponding linear regression equations. The results from both the horizontal and 1% flume slope experiments are lumped together. Due to the smooth shape of the cylinders, they are separate from the remaining shapes. For constant upstream projected area, the ratio F/U^2 is larger for the square-edged elements. Although not shown separately, the horizontal flume corresponds to slightly larger F/U^2 values. This implies that

Equation 2.6 may not be perfectly linear. Separate straight lines for cylinders and square-edged elements represent the data reasonably well.

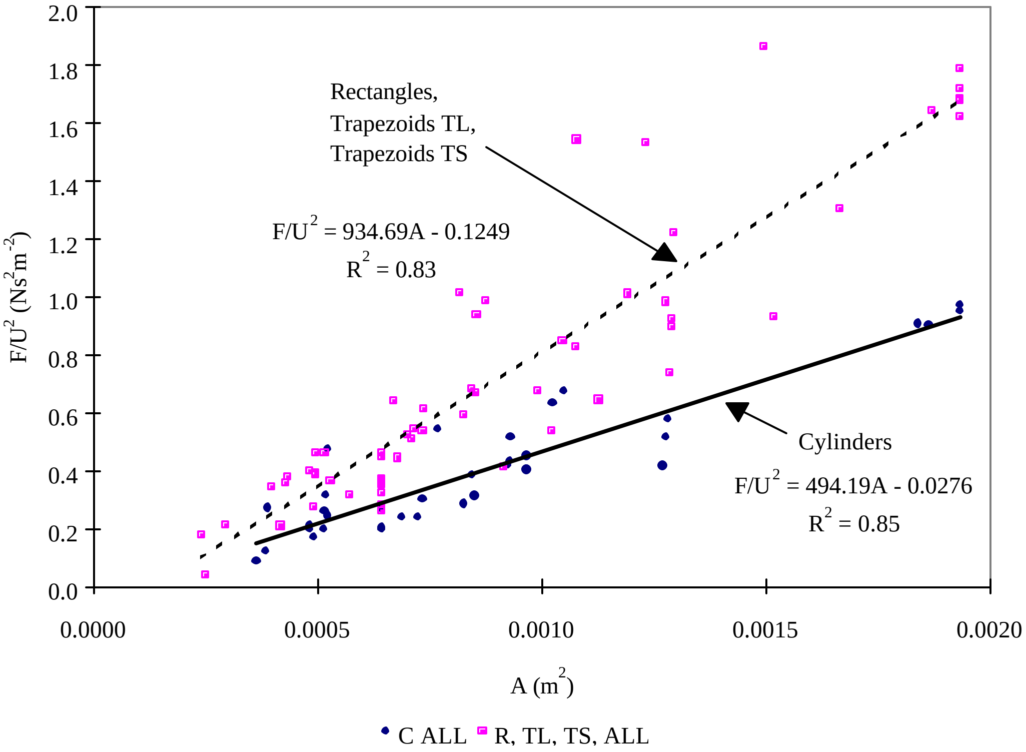

Figure 2.5. F/U^2 Versus A.

The average drag force increases with flow velocity and flow depth, as do the magnitude of the instantaneous fluctuations about the mean. This is demonstrated by the coefficient of variation as defined by Equation 2.1, where $\overline{X}$ is now the average drag force and S_X is the standard deviation of the drag force. The average coefficient of variation increases with increasing flow velocity as shown in Figure 2.6 for the cylinders and all other shapes. The coefficient of variation is larger for the rectangles and trapezoids, than for the cylinders. As expected, the square-edged shapes generate more turbulence leading to larger fluctuations in instantaneous drag forces.

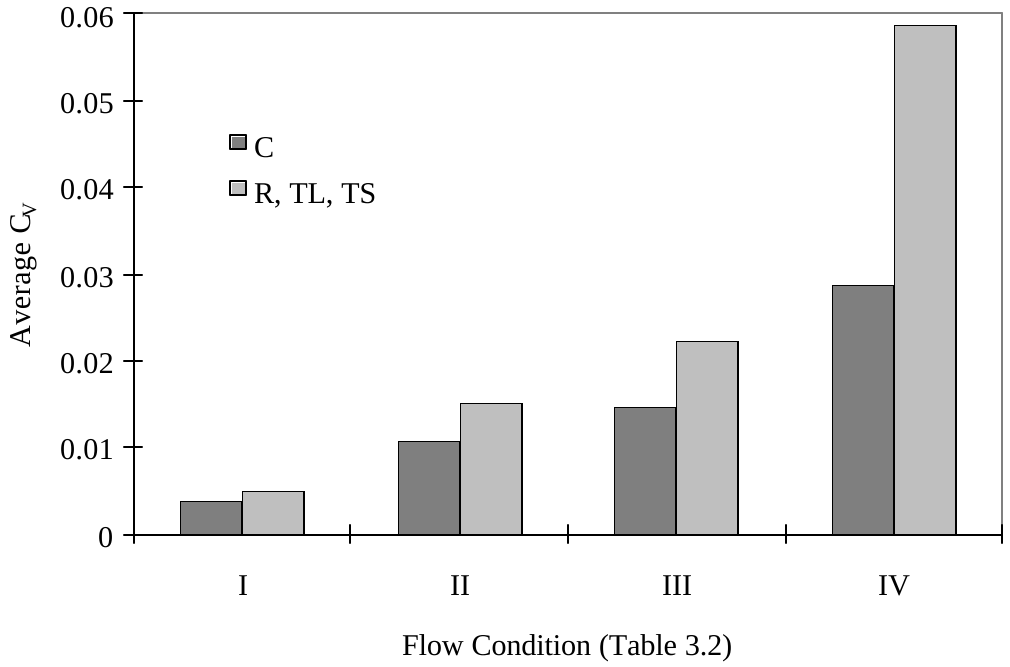

Figure 2.6. Average Coefficient of Variation for Each Flow Condition.

Drag Coefficients

The drag coefficients (C_d) were calculated as

$$C_d = \frac{2F}{rU^2A} \tag{2.7}$$

where F (N) is the drag force, ρ ($kg{\cdot}m^{-3}$)is the density of the fluid, U ($m{\cdot}s^{-1}$) is the mean flow velocity, and A (m^2) is the upstream projected area of the object (Streeter and Wylie, 1985). The drag coefficient is typically represented as a function of Reynolds number, or

$$\text{Re} = \frac{Ud}{u} \tag{2.8}$$

where U is the average velocity ($m{\cdot}s^{-1}$); d is the diameter of the cylinder, the width of the rectangle, or the average width of the trapezoid (m) based on the flow depth; and ν is the kinematic viscosity of water ($m^2{\cdot}s^{-1}$).

The observed drag coefficients are shown in Figure 2.7. Also shown in Figure 2.7, for comparison, are the drag coefficients for a sphere (Morsi, 1972) and the constant value of 1.2 for an infinitely long cylinder (Streeter and Wylie, 1985). As expected, the drag coefficients for the cylinders, rectangles and trapezoids differ from those of spheres. The measured drag coefficients for the cylinders are in close agreement with the reported values of Petryk (1969) which range from 0.7 to 2.0 in a similar range of Froude numbers based on both depth of flow and diameter of element.

Figure 2.8 shows the drag coefficient as a function of flow depth. Separate regression equations were fitted to each type of element. The regression coefficients are given in Table 2.3.

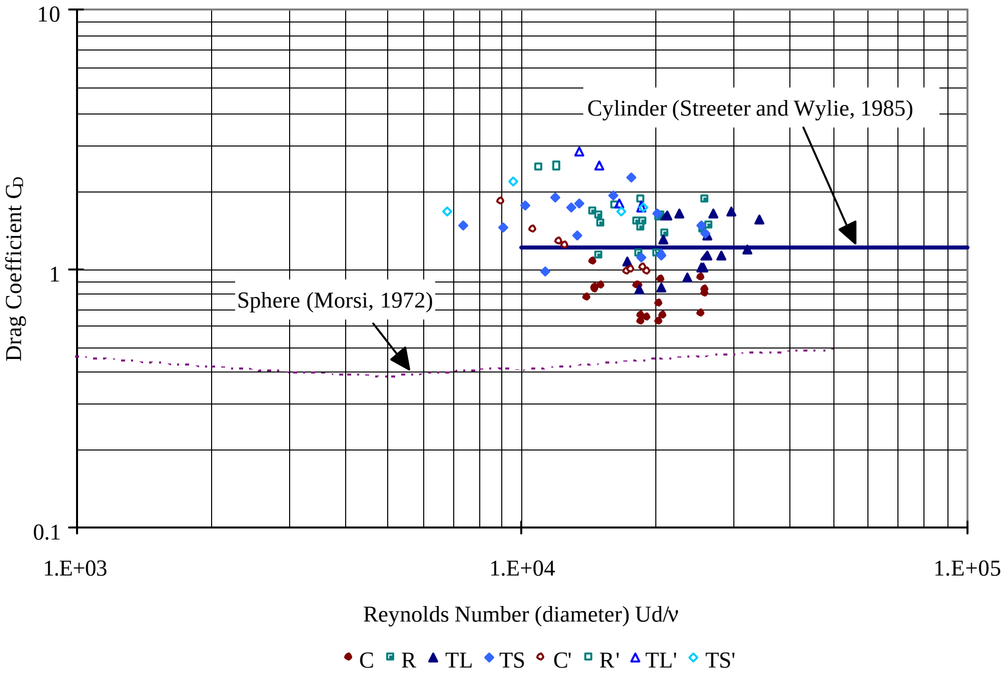

Figure 2.7. Drag Coefficient as a Function of Reynolds Number (All Data).

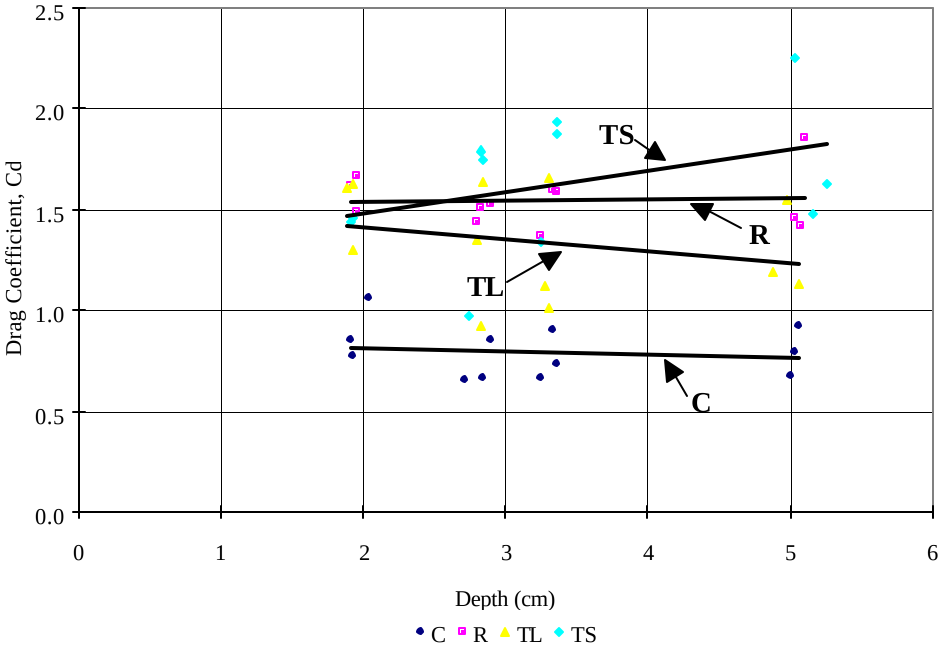

Figure 2.8. Drag Coefficient as a Function of Flow Depth. 1% Flume Slope, Non-Submerged Conditions.

Table 2.3. Regression Parameters Corresponding to Figures 2.8.

Object	Slope	Intercept	R^2
C	-0.016	0.8497	0.022
R	0.0066	1.5241	0.004
TL	-0.0613	1.54	0.071
TS	0.1074	1.2632	0.143

In Chapter 3, a drag coefficient for each of the elements is needed to evaluate the shear partitioning theory. Possible trends with flow depth are therefore important. As shown in Figure 2.8, the drag coefficient is relatively constant with flow depth. However, there is a slight increasing trend for the TS values and a slight decreasing trend for the TL values.

In order to determine if the drag coefficient can be represented by an average value in this range of flow conditions, hypothesis testing is used to determine whether the slope of the drag coefficient versus Reynolds number (depth) is significantly different from zero. A two-tailed t-test is used. The test statistic for the t-distribution is

$$t = \frac{b_1 - k_1}{S_{b_1}} \tag{2.9}$$

where b_1 is the slope of the regression, k_1 is the slope of the null hypothesis (zero), and S_{b1} is the standard error of b_1 or

$$S_{b_1} = \sqrt{S_{b_1}} = \sqrt{\frac{MSE}{\sum_{i=1}^{n} (x_i - \overline{x})^2}} \tag{2.10}$$

The null hypothesis is rejected if $|t_{stat}| > t_{n-2,1-a/2}$. For n = 12 and the 95% confidence interval, $t_{n-2,1-a/2} = 2.228$. This analysis is only for the 1% flume slope and non-submerged values since these are the experimental conditions for the shear stress partitioning presented in Chapter 3. Since, in all cases $|t_{stat}| < t_{n-2,1-a/2}$, the null hypothesis is not rejected. There is insufficient evidence of a trend with depth, and therefore, the data will be represented by an average drag coefficient for each object. The results of the t-test and average drag coefficient for each object is given in Table 2.4.

Table 2.4. T-test Results and Average Drag Coefficients.

	Cylinders	Rectangles	Trap Lb	Trap Sb
t_{stat}	-0.471	0.187	-0.871	1.227
C_D Average	0.80	1.55	1.34	1.63

Error Analysis

The error associated with the drag coefficient is a function of the errors in each variable used to determine the coefficient that is, drag force, upstream projected area, velocity, and fluid density. This section details the analysis used to determine uncertainty in the drag coefficient.

Determining the drag coefficient as Equation 2.7 and substituting

$$U = \frac{Q}{A} = \frac{Q}{bd} \tag{2.11}$$

yields

$$C_D = \frac{2Fd^2b^2}{rAQ^2} \tag{2.12}$$

Errors in measuring width and density are negligible. The resulting relative uncertainty in the drag coefficient is then

$$\frac{u_{C_D}}{C_D} = \sqrt{\left(\left|\frac{u_F}{F}\right|\right)^2 + \left(\left|2\frac{u_d}{d}\right|\right)^2 + \left(\left|\frac{u_A}{A}\right|\right)^2 + \left(\left|2\frac{u_Q}{Q}\right|\right)^2} \tag{2.13}$$

That is, the relative uncertainty is related to the relative error for each term. The error in measured drag force (u_F/F) is a combination of the error associated with using a single calibration equation (described below), and the measurement error associated with the load cell. The error in drag force resulting from the use of a single calibration versus separate calibrations at different locations was determined as

$$Error = \frac{\Delta F_d}{F_d^j} = \frac{F_d^{ALL} - F_d^j}{F_d^j} = \frac{e}{F_d^j} \tag{2.14}$$

where F_d^{ALL} is the drag force computed using the calibration equation from all the data (Figure 2.3) and F_d^j is the drag force using the calibration at location j (locations shown in Figure 2.2). Error (Equation 2.14) ranged from -3.5% to 4.4%. Error associated with the load cell is given by the manufacturer as 2.5%. Total error in measuring drag force is 6.9% (2.5% + 4.4%). Error in the measuring the depth of flow, upstream projected area, and the flow rate are each estimated as 1%. The resulting cumulative uncertainty from Equation 2.13 is 7.3%.

SUMMARY

An important component in understanding shear stress partitioning of vegetated surfaces is the drag force on individual vegetal elements. Instrumentation were developed to measure drag forces on idealized shapes that represent varying geometric properties of vegetation. Four shapes were used to idealize vegetation and to represent variations in upstream frontal area with flow depth. Cylinders were used to represent isolated vertical plant stems and as a comparison to existing data. Rectangles and trapezoids were used to account for constant, increasing and decreasing plant frontal area with flow depth, respectively. Four element heights were considered resulting in a total of 16 element shapes. Drag forces were measured on each shape for flow rates ranging from 0.004 to 0.028 $m^3 \cdot s^{-1}$. This resulted in a total of 80 test scenarios. The flume was horizontal and at a 1% slope. The flow conditions resulted in partial and complete submergence of the elements.

The instrumentation adequately measures drag force on rigid elements. The cylinder drag coefficients are in close agreement with reported values, adding confidence to the measurements. Drag forces are greater on the square-edged, non-cylindrical elements. The ratio of drag force to velocity squared (F/U^2) is well represented by a linear relationship with upstream projected area. The drag coefficients for the square-edged shapes are higher than for the cylinders. The smooth shape of the cylinders provides less resistance to the flow. This results in lower drag force and consequently, lower drag coefficients. Drag coefficients for individual shapes are adequately represented by an average value over the range flow depths investigated. Uncertainty in drag coefficient is 7.3%.

CHAPTER 3
SHEAR STRESS PARTITIONING FOR IDEALIZED VEGETATED SURFACES

INTRODUCTION

This chapter describes the instrumentation system designed and constructed to measure particle shear. It details the methodology and procedures used to measure both components (form and particle) of the shear partition. The total shear is determined by summing these two components. The components of the shear partition are measured over a range of element densities and flow conditions. Finally, the observed partition values are used to evaluate existing shear partitioning theory.

EXPERIMENTAL EQUIPMENT

Hot-Film Anemometry

A constant temperature anemometer (TSI, Inc. Model 1750) and flush-mounted sensor (TSI, Inc. Model 1237W) with immersible probe support (TSI, Inc. Model 1159) were used to measure the boundary shear stress. Feedback circuitry maintains the sensor at a constant temperature. Since a higher flow velocity, and corresponding larger bed shear, cools the sensor more rapidly, a larger voltage is required to maintain the constant temperature of the sensor (Bruun, 1995). The change in voltage can then be related to bed shear by a calibration equation.

Voltage from the anemometer was recorded via a Data Translation DT9804 data acquisition board, SCOPE Version 2.0 Software (Data Translation, 2000) and PC. Voltage was recorded at each measurement location at 200 Hz for 60 seconds.

Laboratory Flume

To collect detailed spatial shear stress measurements, a unique laboratory flume was designed and constructed. This system allowed shear measurements to be made using a single sensor, easily moved to any location within the test array of elements. Because different densities are investigated, it was important to be able to change the measurement locations within test arrays. Alternative designs were considered, including multiple sensors and manually moving a single sensor to fixed locations within the test array. The significant cost (~$1000 per sensor) of the hot-film sensors and probe support (~$600), economically prevented the use of multiple sensors. In addition to the high cost, considerable time and effort is necessary to calibrate multiple sensors. Manually moving a single sensor to a set of fixed positions was eliminated because of the sensitivity and fragile nature of the sensor.

The designed flume used in this experiment includes a single sensor mounted in a movable section of flume floor over the test section. The inner PVC channel is 7.32 m long and 0.38 m wide, with 0.38 m sidewalls. A 0.91 m length of the original channel floor was removed starting 3.7 m from the channel inlet. Slits between the flume floor and the sidewalls exist both upstream and downstream of the test section. A 3.2 mm thick movable aluminum sheet covered with uniform sand (1 mm diameter) glued to its surface provide a floor for the opening. When centered, the movable floor extends 0.17 m upstream and downstream of the opening and 0.25 m to either side of the sidewalls. This distance varies with movement of the floor. The floor slides over the bottoms of the upstream and downstream sections to place the sensor in the specified location. Support columns connect the movable floor to linear motion guide rails above the flume (Braas Company; Eden Prairie, Minnesota). Precise motion of the guide rails in the X and Y direction is through a separate motor drive and gearbox for each axis (Braas Company; Eden Prairie, Minnesota). The motors are driven by MD-2 Dual Stepper Motor Controls (Arrick Robotics; Hurst, Texas) and MD2 software (Arrick Robotics; Hurst, Texas). A schematic of the inner channel, movable floor, and support columns is shown in Figure 3.1. To contain leakage from the slits, a sealed box was constructed around and below the movable floor. The sensor is mounted in a single location in the center of the movable test section floor. By moving the floor, multiple spatial shear measurements are attainable. The total measurement area is 0.078 m^2 (0.28 m by 0.28 m). Access to the sensor mount was obtained via a hole in the bottom of the outside box, sealed with a removable drain plug.

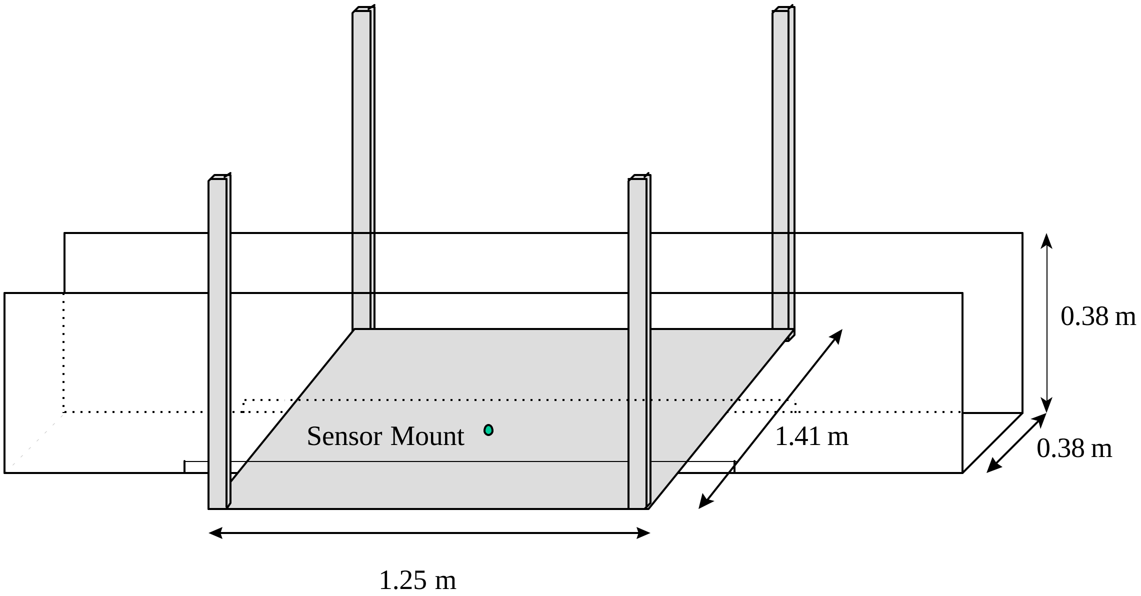

Figure 3.1 Schematic of Flume; Inner Channel, Movable Floor, and Support Columns (Not to Scale).

Water was supplied to the flume inlet tank by two parallel pipes (7.62 cm pipe diameter for low flows and 15.24 cm pipe diameter for high flows) connected in series to a pump and water reservoir (2.8 m^3) located at the flume outlet. The rate of discharge was controlled manually by valves and measured by calibrated orifice plates connected to differential manometers. The slope of the flume was adjusted via screw jacks positioned lengthwise along the flume.

Due to small deflections in the movable floor, and the small step (3.2 mm) upstream and downstream of the test section, there are slight variations in flow depth within the test section. The depth varies approximately 0.5 cm from the upstream edge of the measurement area to the downstream edge. This variation is generally small compared to the non-uniform flow caused by roughness elements.

Elements and Mounting Structure

In order to obtain measurements within the array of elements, the elements were mounted from the top of the flume. The flume floor and sensor move beneath the elements. Figure 3.2 shows a picture of the mounting structure with cylinders attached and mounted in the flume. The cylinders were screwed onto bolts on the underside of the mounting structure. Multiple locations allow for a variety of element densities. The mounting structures were positioned in the flume and clamped to the sidewalls, such that elements were as close to the flume floor (within 0.32 cm) as possible without interfering with the movement of the floor underneath the elements. Although this does not precisely model vegetation connected to the ground, it gives a close approximation and reasonable first step at investigating the process. The overall layout shown in Figure 3.3 illustrates the entire system.

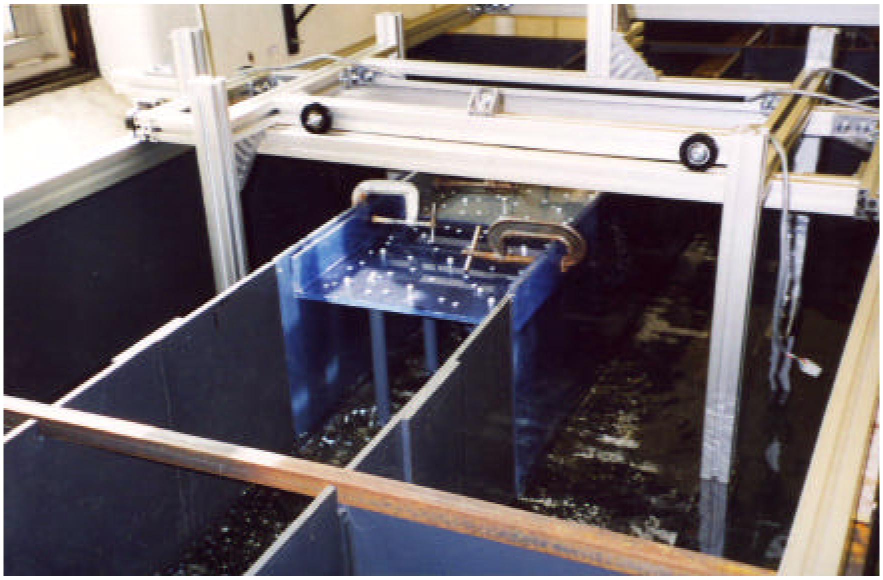

Figure 3.2. Element Mounting Structure in Flume.

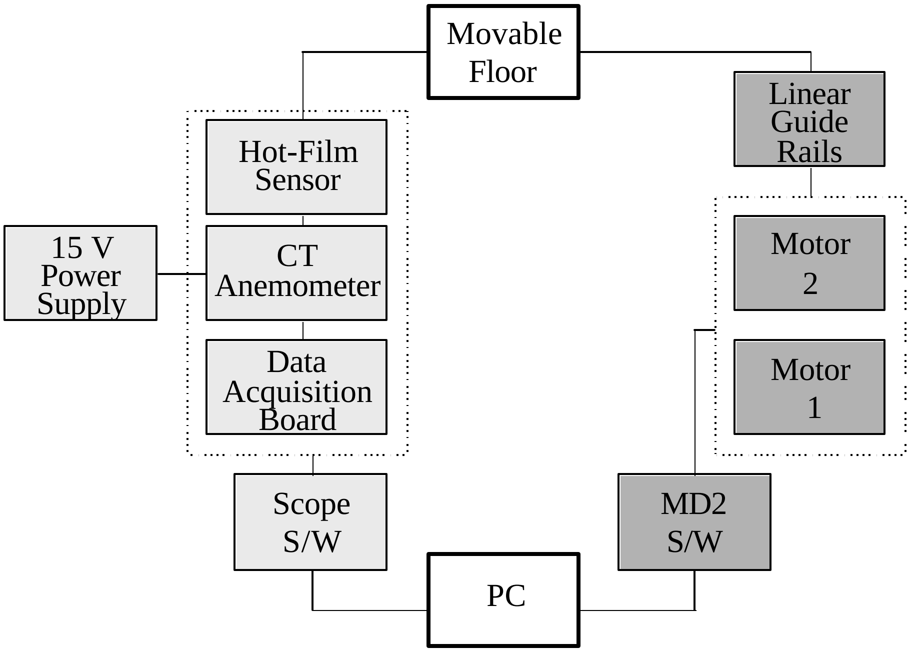

Figure. 3.3. Layout of Flume and Instrumentation System

EXPERIMENTAL PROCEDURE

Overview of Tests

The four idealized shapes shown in Figure 2.4 were used to represent geometric characteristics of vegetation. The height of the elements was 7.62 cm. Two cylinder diameters were used: 0.95 cm and 2.54 cm. Again, the width of the rectangle was 2.54 cm and the bases of the trapezoids were 0.95 and 4.13 cm. A rigid rod was used to connect the element to the mounting structure. Letters are used to designate element shape and the notation is as follows: 0.95 and 2.54 cm diameter cylinders are SC and C, respectively; rectangles, trapezoids with large base oriented at the bottom, and trapezoids with small base oriented at the bottom, are R, TL, and TS, respectively.

Three element densities were investigated using cylinders: 1, 4, and 9 elements per 0.145 m^2. The notation used to describe element density is a number (1, 4, or 9) which corresponds to the number of elements per 0.145 m^2. These density scenarios correspond to diameter/spacing ratios ranging from

0.039 to 0.20. Hayes et al. (1979) reports diameter/spacing ratios of 0.05 to 0.09 for grass filters. The effect of variations in upstream frontal area with depth (rectangular and trapezoidal shapes) was investigated for a single density of 1 element per 0.145 m^2. A schematic of the test arrays is shown in Figure 3.4.

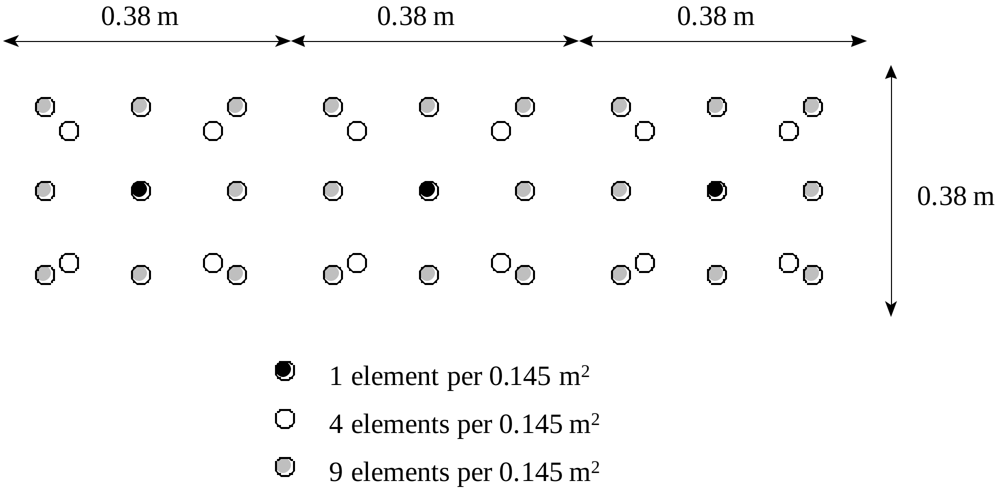

Figure 3.4. Element Densities; Measurements in Center Section.

For each test scenario, two flow rates were used: 0.0045 m^3·s^{-1} and 0.0105 m^3·s^{-1}, which correspond to flow conditions A and B, respectively. This combination of element shape, density, and flow conditions corresponds to a total of sixteen test scenarios. Each test scenario is designated by a letter (corresponding to element shape), followed by a number (corresponding to element density), and ends with a letter (corresponding to the flow condition). For example, for the 2.54 cm cylinders at an element density of 1 element per 0.145 m^2, and flow rate of 0.0045 m^3·s^{-1}, is designated as C1A. A summary of the test scenarios is given in Table 3.1.

Table 3.1. Test Scenarios and Experimental Flow Conditions.

Scenario Reference	Description (Number of elements/ $0.145m^2$)	Flow Rate Q ($m^3 \cdot s^{-1}$)	Average Depth (m)	Diameter/ Ave. Width (cm)
C1A	1 Cylinder	0.0045	0.025	2.54
C1B	1 Cylinder	0.0105	0.035	2.54
R1A	1 Rectangle	0.0045	0.024	2.54
R1B	1 Rectangle	0.0105	0.038	2.54
TL1A	1 Trapezoid (Large)	0.0045	0.025	3.61
TL1B	1 Trapezoid (Large)	0.0105	0.038	3.33
TS1A	1 Trapezoid (Small)	0.0045	0.025	1.47
TS1B	1 Trapezoid (Small)	0.0105	0.036	1.69
C4A	4 Cylinders	0.0045	0.026	2.54
C4B	4 Cylinders	0.0105	0.046	2.54
SC4A	4 Cylinders	0.0045	0.022	0.95
SC4B	4 Cylinders	0.0105	0.036	0.95
C9A	9 Cylinders	0.0045	0.030	2.54
C9B	9 Cylinders	0.0105	0.058	2.54
SC9A	9 Cylinders	0.0045	0.024	0.95
SC9B	9 Cylinders	0.0105	0.041	0.95

For each test run, the elements were attached to the mounting structures and positioned in the flume. Elements extended 0.381 m upstream and downstream of the measurement area. Due to changes in element placement, each element density required a separate sampling scheme for the collection of spatially varied shear stress.

Calibration of Hot-Film Sensor

Due to errors that can result from sensor contamination and changes in water temperature (Bruun, 1995), frequent calibration is required to ensure accurate measurements. The sensor was calibrated by varying the flow rate through the calibration pipe. A schematic of the hot-film sensor calibration set-up is shown in Figure 3.5. Ten flow rates were used. For each flow rate, the piezometric gradient was measured and the voltage from the anemometer and water temperature were recorded. Voltage was sampled for at 200 Hz for 60 seconds. The average boundary shear stress for fully developed turbulent pipe flow was calculated as

$$t = rgRS \tag{3.7}$$

where τ (Pa) is the average boundary shear stress, ρ ($kg \cdot m^{-3}$) is the density of the fluid, g ($m \cdot s^{-2}$) is acceleration due to gravity, R (m) is the hydraulic radius, and S ($m \cdot m^{-1}$) is the piezometric gradient. The following nonlinear calibration equation was fitted to the data

$$\frac{V^2}{(T_S - T_W)} = At^B + C \tag{3.8}$$

where V is the time-averaged voltage, τ (Pa) is the average boundary shear stress from Equation 3.7, ΔT (°C) is the operating temperature of the sensor minus the water temperature, and A, B, and C are fitted parameters. Similar calibration procedures were used by Robinson (1989) and Garcia et al. (1998).

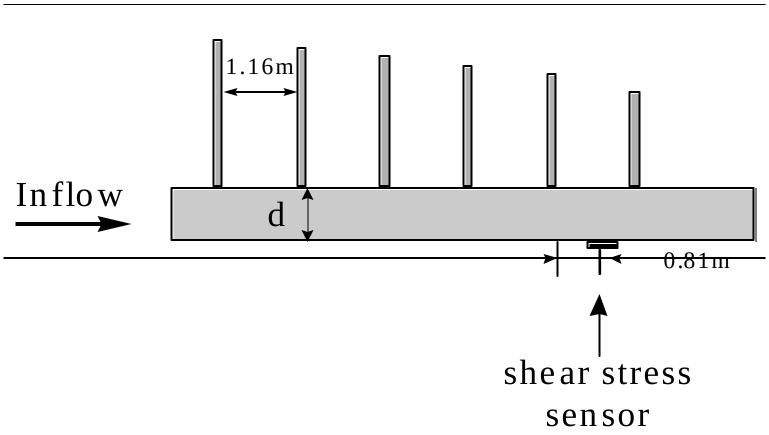

Figure 3.5. Hot-film Sensor Calibration Pipe.

The sensor was calibrated prior to the experiments as well as three additional times throughout the period of data collection. The results of the calibrations are shown in Figure 3.6. In general the calibrations were similar. Table 3.2 shows the chronological order of calibrations and experiments, as well as the calibration parameters. The calibration parameter, B, is normally assumed constant for individual probes (Bruun, 1995). This value was a fitted parameter for this study. It remained relatively constant throughout the span of data collection, adding confidence to the reliability of the measurements and the probe working properly.

Uncertainty in the calibration curve was assessed using the 95% confidence intervals. Based on this analysis, the measurement resolution of bed shear measurements was estimated as 0.06 Pa for small shear values (1 Pa) and 0.35 Pa for large shear values (6 Pa). The measurement resolution of the ratio of shear to average bed shear was estimated as 0.012 and 0.074 for small and large shear values, respectively.

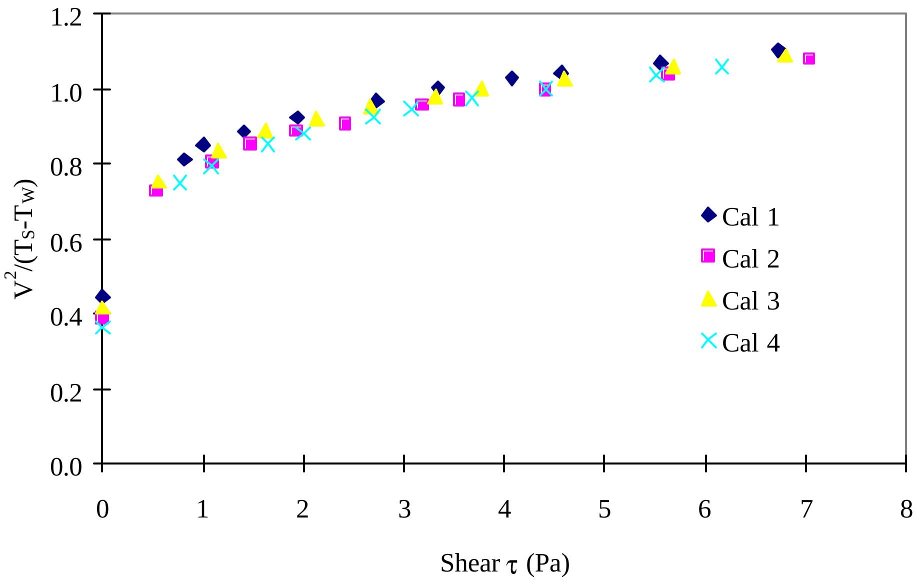

Figure 3.6. Hot-Film Anemometer Calibrations.

Table 3.2. Chronological Order of Calibrations and Test Runs

Calibration	Test Runs	Date	Calibration Parameter			
			A	B	C	R^2
Calibration 1		6/27/01	0.400	0.264	0.445	0.999
	C1A, C1B, TS1A, TS1B, R1A, R1B, TL1A, TL1B	6/28/01 to 7/2/01				
Calibration 2		7/3/01	0.413	0.268	0.386	0.999
	C9A, C9B	7/11/01				
Calibration 3		7/11/01	0.408	0.267	0.417	0.999
	C4A, C4B, SC4A, SC4B, SC9A, SC9B	7/16/04 to 7/18/01				
Calibration 4		7/19/01	0.425	0.275	0.363	0.999

Sampling Locations and Frequency

A sampling scheme was selected on the assumption that more locations are needed closer to the element because of a greater change in bed shear in this region. Due to constraints in the lifetime of the sensor, it was important to keep the total number of measurements at a maximum of approximately 35-45 per test scenario to ensure that all data could be collected within the life of the sensor. For the single densities, the sampling was determined such that the spacing between measurement locations doubles with distance from the element.

The first measurement was set at a distance of 1.5 cm from the edge of the cylinder (2.54 cm diameter). The distance over which the remaining measurements were taken, L (m), is defined as

$$L = \Delta x_1 + \Delta x_2 + \ldots \Delta x_n \qquad (3.9)$$

where the Δx's are the spacings between measurement locations. The second distance is twice the first distance, or

$$\Delta x_2 = 2\Delta x_1 \qquad (3.10)$$

Likewise for the third location

$$\Delta x_3 = 2\Delta x_2 = 2 \cdot 2 \cdot \Delta x_1 = 2^{3-1}\Delta x_1 \tag{3.11}$$

and therefore conclude that

$$\Delta x_{n_M} = 2\Delta x_{n_M - 1} = 2^{n_M - 1}\Delta x_1 \tag{3.12}$$

By substituting these relationships into Equation 6.9,

$$L = \Delta x_1 \left(1 + 2^{2-1} + 2^{3-1} + \ldots + 2^{n_M - 1}\right) = \Delta x_1 S_T \tag{3.13}$$

where S_T is the summation term defined as

$$S_T = \left(1 + 2^{2-1} + 2^{3-1} + \ldots + 2^{n_M - 1}\right) \tag{3.14}$$

The summation term can be simplified by subtracting $S_T/2$ from both sides and rearranging terms to obtain

$$S_T = -1 + 2\left(2^{n_M - 1}\right) = 2^{n_M} - 1 \tag{3.15}$$

Substituting this into Equation 6.13 yields

$$\Delta x_1 = \frac{L}{2^{n_M} - 1} \tag{3.16}$$

where, again L (m) is the total distance from the first measurement location to the furthest measurement location and n_M is the total number of measurements over the distance L. L was selected as 11.2 cm for the single density design.

Similar methodology was used to determine the sampling schemes for the 4 and 9 elements per 0.145 m^2. Here the methodology was applied to the perpendicular distances between cylinders. Fewer locations were used on the diagonals between elements so as not to exceed the maximum number of measurement locations (35-45). The measurement and element locations are shown for the 3 densities in Figure 3.7.

To investigate the impact of sampling density on average shear stress, 24 additional measurement locations were added to the scheme for the rectangle (scenario R1B). This sampling scheme is shown in Figure 3.7B. These additional locations were used to estimate the magnitude of the error in determining the average bed shear based on only 32 measurement sites as normally done and is shown in Figure 3.7A. The rectangular shape was used because it had a higher form drag, thereby increasing the expected variability within measurements. Using 32 measurements resulted in an average bed shear of 1.82 Pa while 56 locations resulted in an average bed shear of 1.84 Pa. These averages were determined over the measurement area only and result in an error of 1%. From this evaluation, the 32 site locations appear adequate to determine average bed shear, at least for the single density tests.

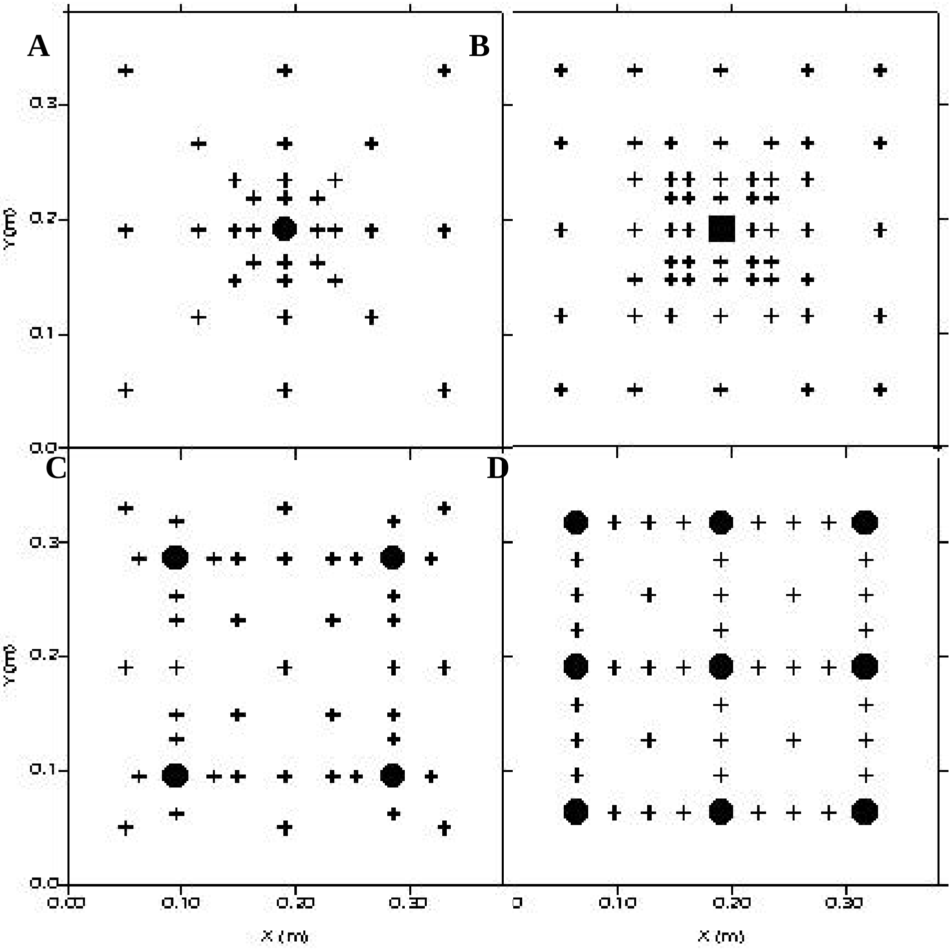

Figure 3.7. Sampling Schemes. A) 1 element per $0.145m^2$, B) 1 element per $0.145m^2$ with 24 additional sampling locations, C) 4 elements per $0.145m^2$, D) 9 elements per $0.145m^2$.

In addition to spatial sampling, an appropriate sampling frequency is needed to evaluate the turbulent characteristics of shear stress. Richardson and McQuivey (1968) measured turbulent velocities in an open channel and found that approximately 60% of the energy is concentrated in frequencies less than

10 Hz with very little power in frequencies greater than 100 Hz. This trend was similar for both smooth and rough boundaries. In a study of hydraulic stresses on overfall boundaries, Robinson (1989) sampled at 200 Hz and found the observed flow frequencies were generally less than 50 Hz.

The Nyquist criterion requires the sampling rate be at least twice the rate of the highest frequency of interest. The Nyquist frequency is that frequency that can adequately be represented with the chosen sampling frequency. The frequency response of the TSI, Inc. constant temperature thermal anemometer (Model 1750) is 100 kHz, which is more than adequate for measuring turbulent characteristics for this study. Based on previous studies of open channel flow, the sampling frequency for this study was selected as 200 Hz.

Measurement of Form and Particle Shear

In order to determine the shear partition, both the particle shear and the form shear were measured for each of the sixteen test scenarios. The elements were positioned in the flume and the flume floor was positioned such that the sensor was at the first measurement location. The pump was then turned on and water was allowed to recirculate through the flume. Once steady state conditions were reached (as measured by a constant flow depth), the flow rate was recorded, and voltage from the anemometer was sampled at 200 Hz for 60 seconds. The flume floor and sensor were moved to the next measurement location, steady state conditions were reached, and the voltage sampled from the anemometer. This procedure was repeated until the voltage had been sampled at all measurement locations.

After measuring the shear stress for each test scenario, the drag force on individual elements within the test array was measured for the same flow conditions. Please refer to Chapter 2 for details on the instrumentation and procedure for measuring drag force on individual vegetal elements. In order to do this, the elements (with the exception of the element whose drag force was being measured) were mounted to the test section floor. A separate drag force measurement was made on each element within the test array. Total form drag was determined by summing the individual drag on each element within the array. Figure 3.8 shows the total form drag as a function of element density. As expected, drag force increases with increasing density. All shapes are included which explains some of the scatter.

Finally, the flow depth was measured using a pointgage at 3 or 4 cross-sections within the array, depending on element density. The entire procedure was repeated for the second flow rate. The 16 test scenarios resulted in a total of 604 particle shear measurement locations (each containing 12,000 shear measurements) and 60 individual element drag force measurements.

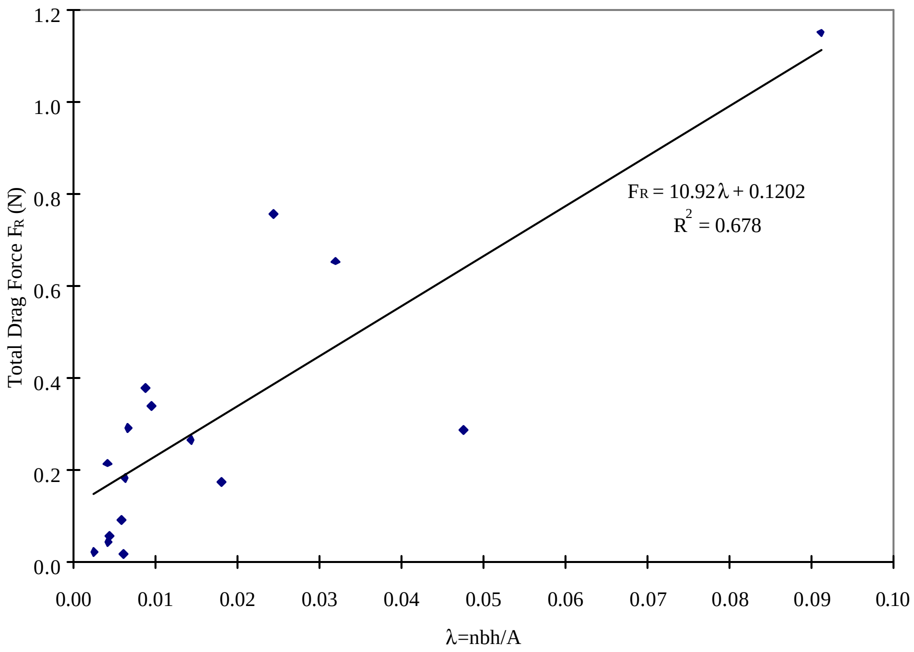

Figure 3.8. Total Element Drag as a Function of Element Density.

RESULTS AND DISCUSSION

Particle and Form Shear

The average particle shear was determined by estimating the contour intervals and obtaining the average surface shear using the software SURFER 5.0 (Golden Software, Inc. 1993). Visual inspection indicated that the contour lines were representative of the observed values. Contours were extended beyond the measurement area to the flume walls. A visual check of the contour lines showed that extending the contour area to the flume walls did not change the locations of the contours. Also, on average, the difference in computed average bed shear was within 4.5%, with this percentage decreasing as element density increased.

Figure 3.9 and 3.10 show the contours of actual shear measurements for test scenarios C1A and C1B. Flow is in the direction of increasing X. Upstream of the cylinder, flow velocity decreases as it approaches the cylinder. Flow velocity is also reduced downstream of the cylinder. This results in areas of low shear upstream and downstream of the cylinder. Areas of higher shear exist on either side of the cylinder as the flow accelerates around the cylinder. Figures 3.11 and 3.12 show the contours for test scenarios SC4A and SC4B. Again, shown particularly for the high flow condition in Figure 3.12, low shear exists upstream and downstream of the cylinders with areas of higher shear as the flow accelerates between the cylinders. The contours for the remaining scenarios are given in the Appendix A.

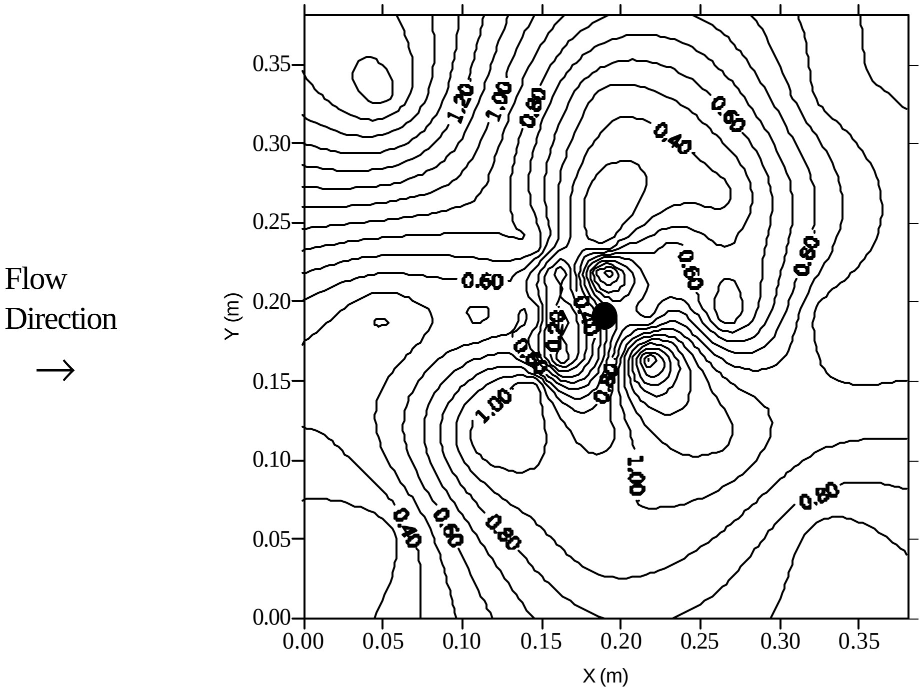

Figure 3.9. C1A Shear Stress (Pa) Contours. Q = 0.0045$m^3 \cdot s^{-1}$,
Average Shear = 0.8 Pa, Minimum Measured = 0.1 Pa, Maximum Measured = 1.76 Pa.

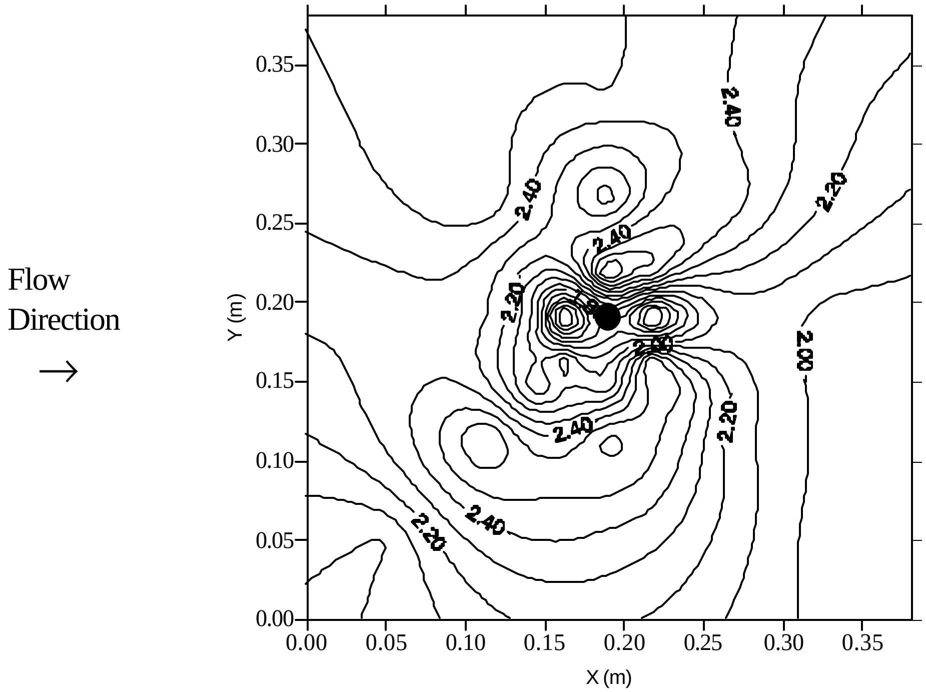

Figure 3.10. C1B Shear Stress (Pa) Contours. Q = $0.010 m^3 \cdot s^{-1}$,
Average Shear = 2.27 Pa, Minimum Measured = 1 Pa, Maximum Measured = 2.9 Pa.

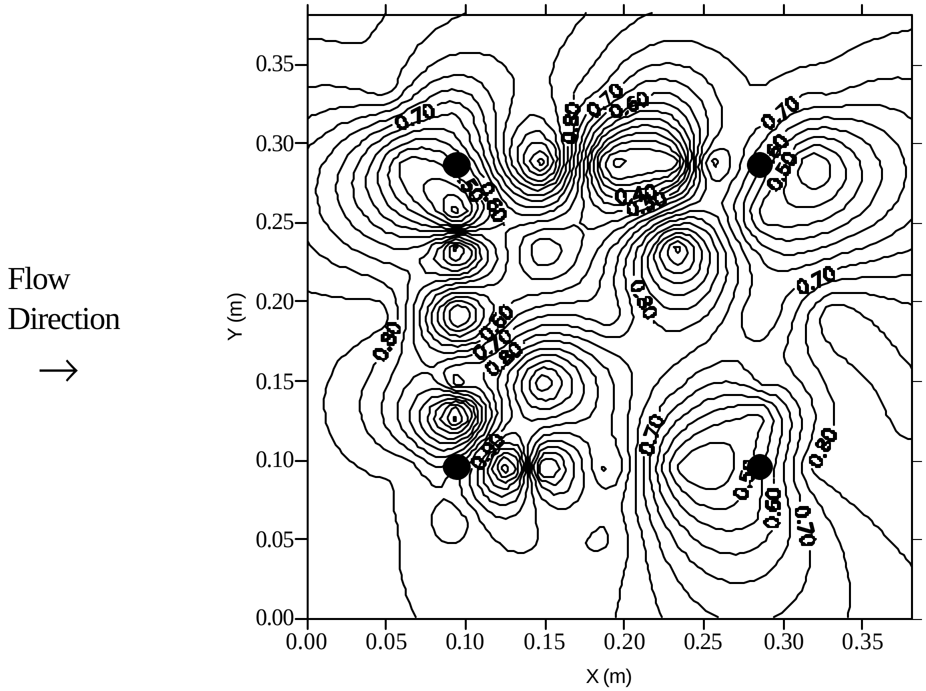

Figure 3.11. SC4A Shear Stress (Pa) Contours. Q = $0.0045 m^3 \cdot s^{-1}$,
Average Shear = 0.73 Pa, Minimum Measured = 0.16 Pa, Maximum Measured = 1.3 Pa.

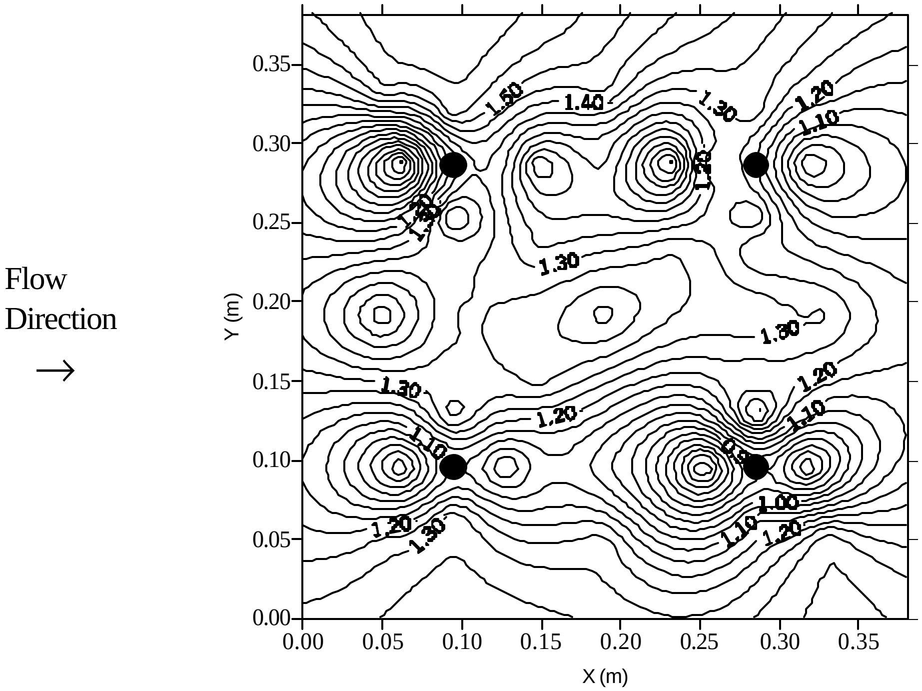

Figure 3.12. SC4B Shear Stress (Pa) Contours. Q = 0.010 $m^3 \cdot s^{-1}$,
Average Shear = 1.24 Pa, Minimum Measured = 0.5 Pa, Maximum Measured = 1.6 Pa.

The total form shear was determined by summing individual element drag within the test array and dividing by the area of the test array (0.145 m^2). Total shear is the sum of particle shear and form shear. The results are given in Table 3.3.

Table 3.3. Results: Scenario, λ, β, τ_S, τ_R, τ_S/τ.

Scenario	λ	β	τ_S	τ_R	τ_S/τ
C1A	0.0043	147	0.80	0.40	0.664
C1B	0.0062	178	2.27	1.27	0.642
R1A	0.0042	285	0.96	0.31	0.757
R1B	0.0066	345	1.80	2.01	0.472
TL1A	0.0061	246	0.99	0.12	0.889
TL1B	0.0088	298	1.72	2.61	0.397
TS1A	0.0025	279	1.25	0.16	0.888
TS1B	0.0042	338	2.07	1.49	0.582
C4A	0.0181	147	0.83	1.21	0.407
C4B	0.0319	178	0.99	4.52	0.179
SC4A	0.0058	147	0.73	0.64	0.535
SC4B	0.0095	178	1.24	2.35	0.346
C9A	0.0476	147	0.78	1.99	0.282
C9B	0.0912	178	1.19	7.94	0.130
SC9A	0.0143	147	0.76	1.84	0.293
SC9B	0.0244	178	0.97	5.22	0.156

Shear Stress Partition Theory

The shear stress partitioning theory described by Raupach (1992) provides a predictive relationship for estimating the fraction of total shear stress acting on the surface. A significant advantage of Raupach's approach in comparison to other partitioning theories (Arya, 1975; Wooding et al., 1973) is that it is free of adjustable constants. The theory was developed for wind erosion and is applied to water with modifications. The ratio of surface shear to total shear predicted by Raupach (1992) is

$$\frac{t_s}{t} = \frac{1}{1+b\,l} \tag{3.17}$$

where τ_s is the surface shear stress, τ is the total shear stress, β is the ratio of element drag coefficient to particle drag coefficient without elements, and λ is the roughness density, or

$$b = \frac{C_R}{C_S} \tag{3.18}$$

$$l = \frac{Nbh}{A} \qquad (3.19)$$

where C_R is the drag coefficient for a single element, C_S is the particle drag coefficient without elements, N is the number of elements, b and h are the height and width of the element, respectively, and A is the total ground surface area.

As an alternative theoretical approach, Wooding et al. (1973) suggest that $(\tau_R/\tau)^{1/2}$ varies linearly with $\log(1/\lambda)$ or

$$\left(\frac{t_R}{t}\right)^{1/2} = A\log\left(\frac{1}{l}\right) + B \qquad (3.20)$$

Application of Equation 3.20 requires that two parameters be fitted to the experimentally observed data.

The mean squared error is used to evaluate the predictive theories and is defined as

$$MSE = \frac{\sum_{i=1}^{N}\left(x_{Oi} - x_{Pi}\right)^2}{N} \qquad (3.21)$$

where x_{Oi} and x_{Pi} are defined as the observed and predicted values of the ratio of particle shear velocity (u_{*S}) to total shear velocity (u_*), or

$$\frac{u_{*S}}{u_*} = \frac{\sqrt{t_S / r}}{\sqrt{t / r}} = \left(\frac{t_S}{t}\right)^{1/2} \qquad (3.22)$$

Evaluation of Shear Partition Theories

In Raupach's original development, the parameter β (Equation 6.17) is assumed constant. For the open channel flow conditions of this study, the value was adjusted for flow conditions. Details of this adjustment are given first. The theories of Raupach (1992) and Wooding et al. (1973) are then evaluated with the observed values.

Let's consider the particle drag coefficient without elements defined as

$$C_S = \frac{t_S}{rU^2} \tag{3.23}$$

where U ($m{\cdot}s^{-1}$) is the average velocity (Raupach, 1992). The value of C_s was determined indirectly from measurements of bed shear and velocity for flow conditions without form elements. For open channel flow, the average boundary shear stress is

$$t_S = rgRS \tag{3.24}$$

where ρ ($kg{\cdot}m^{-3}$) is the density of water, g ($m{\cdot}s^{-2}$) is acceleration due to gravity, R (m) is the hydraulic radius, and S ($m{\cdot}m^{-1}$) is the slope. For a constant slope of 1%, the flow rate was varied from 0.003 to 0.027 $m^3{\cdot}s^{-1}$. Flow depth was measured with a pointgage equal distance upstream and downstream of the midpoint of the test section (spanning a distance of 0.94 m). Average boundary shear was calculated from Equation 3.24. Average velocity ($m{\cdot}s^{-1}$) was determined as

$$U = \frac{Q}{A} \tag{3.25}$$

where Q is flow rate ($m^3{\cdot}s^{-1}$) and A is cross-sectional area of flow (m^2). Particle drag coefficient without elements was then calculated using Equation 3.23. The results are shown in Figure 3.13. The best-fit nonlinear equation is

$$C_S = 0.0016Q^{-0.2266} \tag{3.26}$$

where C_S and Q are previously defined, and $R^2 = 0.95$.

Although observed values in Figure 3.13 are used in this study, an estimate of C_S using widely reported Manning's n is desirable for field application. By using Manning's equation

$$U = \frac{1}{n} R^{2/3} S^{1/2} \tag{3.27}$$

where n is the dimensionless roughness coefficient and the constant (1) has units of $m^{1/3}{\cdot}s^{-1}$ (Streeter and Wylie, 1985) to determine average flow velocity and by using Equation 3.24 for bed shear, C_S can be defined directly from Equation 3.23 as

$$C_S = \frac{n^2 g R^{-1/3}}{1} \tag{3.28}$$

and C_S is now defined for known n and R values. Manning's roughness coefficient was determined experimentally by measuring the flow depth across the test section for various flow rates. A value of n=0.012 was calculated from Equation 3.24. The C_S values computed by Equation 3.28 for n=0.012 are compared to actual measurements in Figure 3.13.

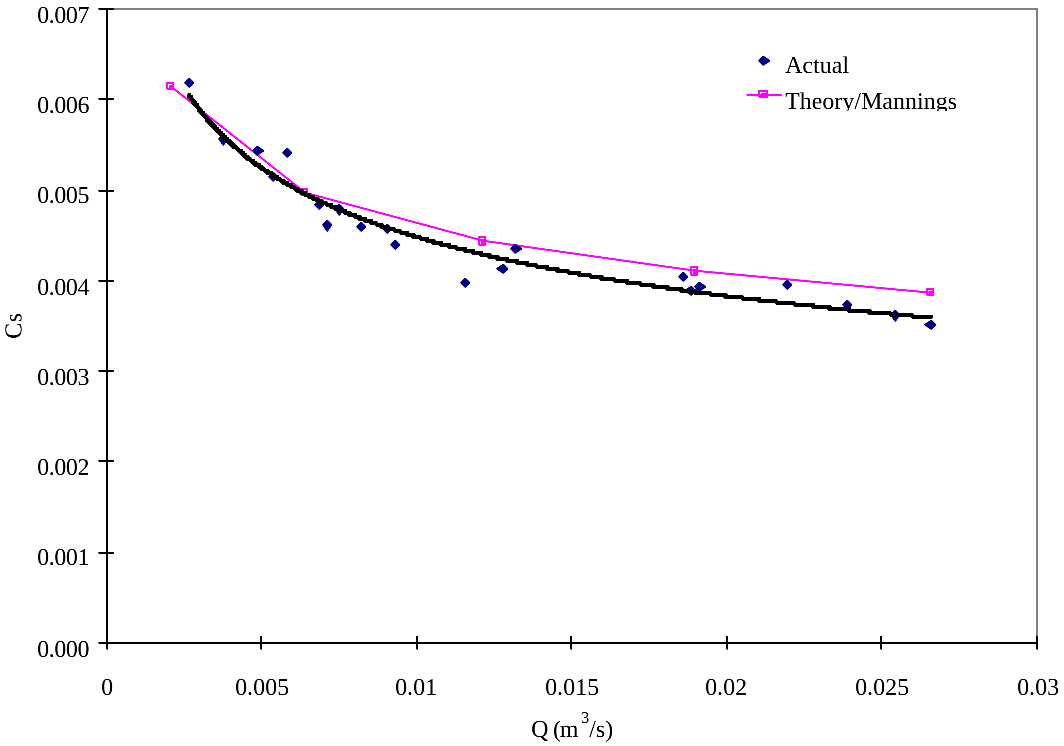

Figure 3.13. Particle Drag Coefficient as Function of Flow Rate.

At low flow rates where the rough floor contributes the majority of the overall shear, the values are in close agreement. As flow rate (and depth) increases and the smooth side walls contribute more to the average boundary shear, the actual values are, in general, slightly less than theoretical values.

As the particle drag coefficient varies with flow depth and velocity, so does the parameter β (assuming a constant C_R value). As determined in Chapter 2, the average drag coefficient varies with element shape and is relatively independent of flow depth. The average drag coefficients reported in Chapter 2 for cylinders, rectangles, trapezoids-large base, and trapezoids-small base are 0.8, 1.55, 1.34, and 1.63; respectively. The resulting relationship for β is a function of flow depth as shown in Figure 3.14.

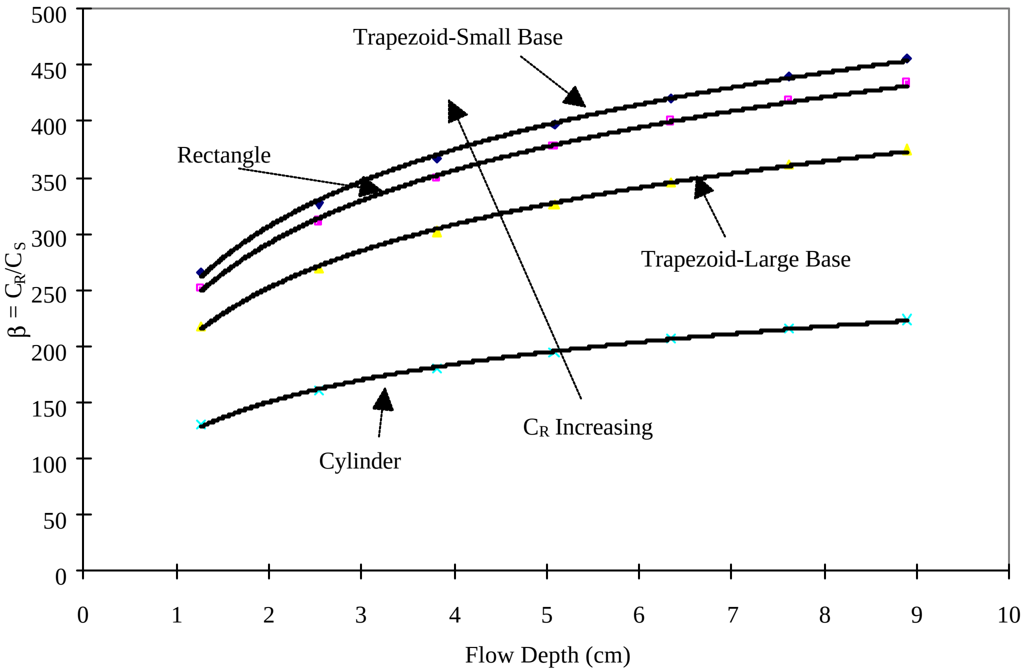

Figure 3.14. β Versus Flow Depth, C_R = 0.8, 1.34, 1.55, and 1.63.

According to Raupach (1992), the shear stress partition given in Equation 3.17 varies with roughness density (λ) and β which is dependent on the flow depth. The solution of Raupach's equation, defined using shear velocities, is shown in Figure 3.15, as a function of λ and for four values of β.

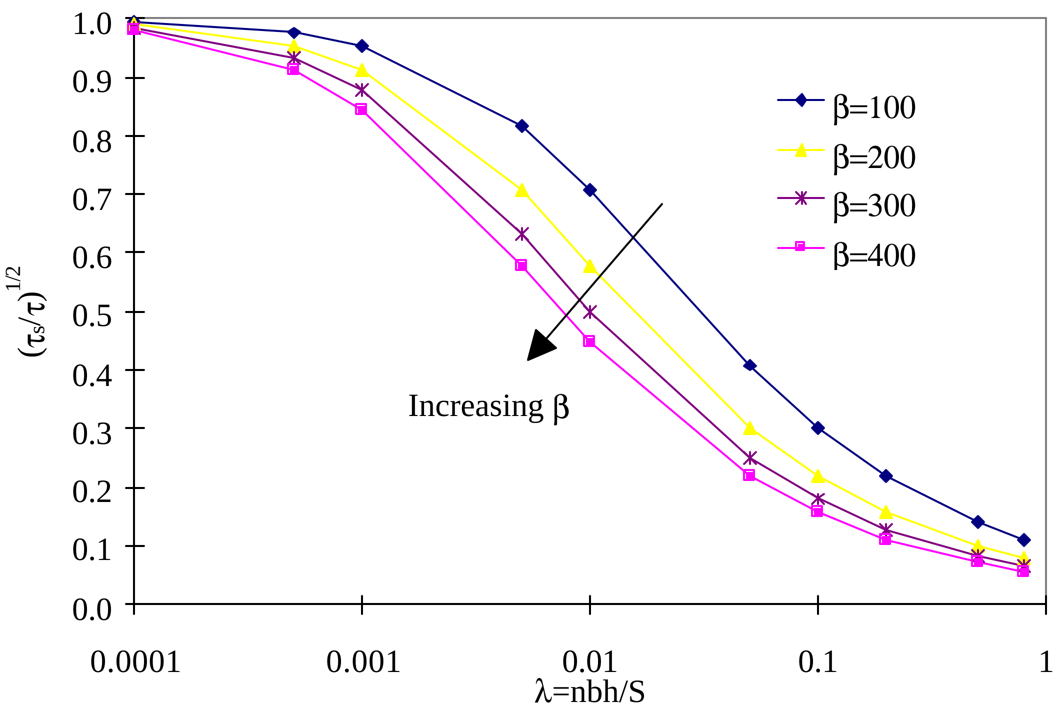

Figure 3.15. Shear Partition as a Function of Roughness Density; β = 100, 200, 300, and 400.

For wind erosion field conditions, β is often assumed constant (Wyatt and Nickling, 1997) and the partition is then a function of λ only. However, as previously described, β varies with flow depth. Therefore, a unique function is obtained for the product of β and λ.

The prediction of shear partition using the theory of Raupach (1992) for the conditions of the experimental runs is shown in Figure 3.16. The observed values for the sixteen runs are also shown in Figure 3.16. These values have accounted for differences in C_R based on element shape. The measured results are reasonably represented by the theory of Raupach (1992).

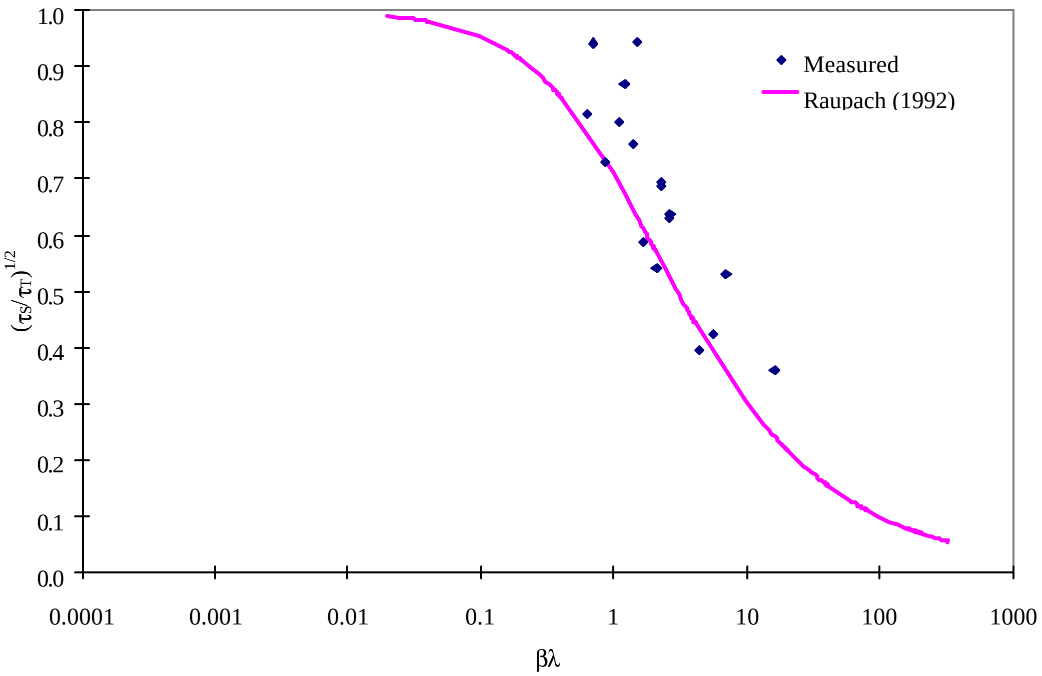

Figure 3.16. Shear Partition Theory (Raupach, 1992) and Measured Values.

According to Raupach (1992), the shear partition is insignificant (τ_S/τ very small) when λ is greater than 0.03 to 0.1. Marshall (1971) found λ ranged from 0.0209 to 0.0417 when surface shear became negligible. The observed partition (τ_S/τ) reaches values of 0.1 to 0.2 for roughness densities in the range of 0.03 to 0.09, which is similar to those studies.

The prediction of the shear partition using the theory of Wooding *et al*. (1973), as described in Equation 3.20, for the conditions of the experimental runs is shown in Figure 3.17. Also shown in Figure 3.17 are the observed values for the sixteen runs.

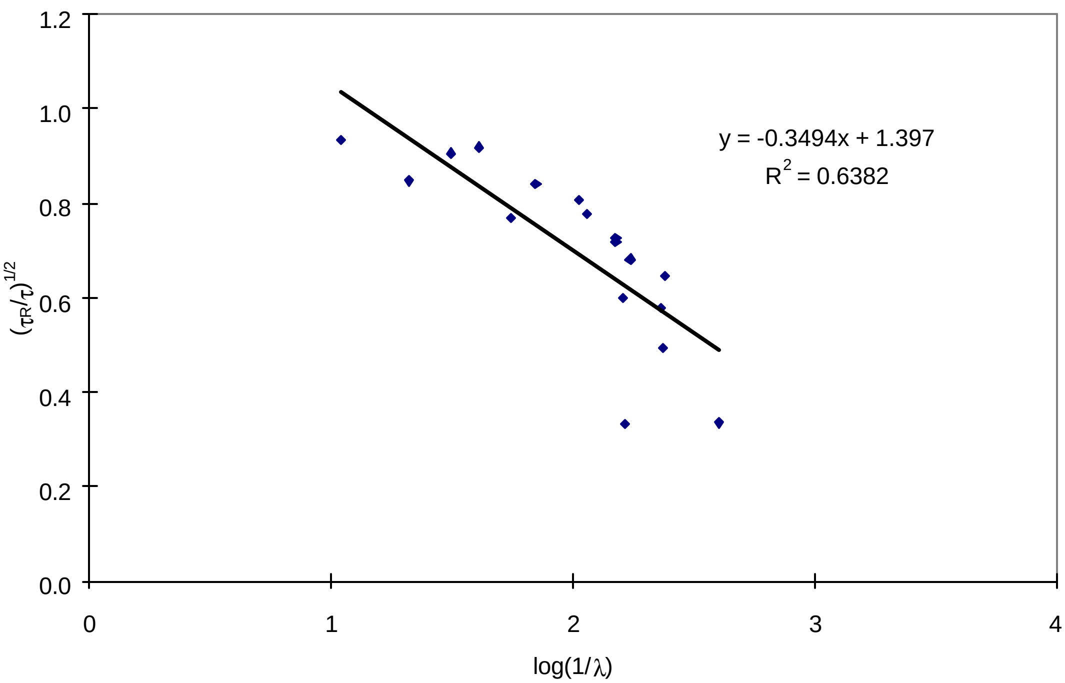

Figure 3.17. Wooding et al., (1973) Linear Prediction of Shear Partition.

The MSE as determined from Equation 3.21 is 0.018 and 0.017 for the theories of Raupach (1992) and Wooding et al., (1973), respectively. The MSE for the theory of Wooding et al. (1973) is smaller than the MSE of Raupach (1992)'s theory. This is expected because the equation is fitted to the data directly. Although both provide similar MSE, a significant advantage of the Raupach (1992) theory is that it is free of adjustable constants. Another limitation of Wooding et al., (1973) is that it predicts values of $(\tau_R/\tau)^{1/2} > 1$, which is physically impossible.

SUMMARY

Vegetation is an important erosion control measure that protects the soil surface from raindrop impact. Vegetation also partitions the total shear of the flow into one component acting on the vegetation (form shear) and the remainder acting on the intervening soil surface (particle shear). It is the portion acting on the soil surface that is responsible for particle detachment by surface runoff. The ratio of particle shear to total shear is referred to as the shear stress partition.

This study evaluated the partition for idealized vegetation in overland flow. Idealized shapes were used to model the geometric characteristics of vegetation. A unique laboratory flume with a movable test section floor was designed and used in conjunction with hot-film anemometry to measure the spatial and temporal variations in particle shear over a range of element densities. Form shear was measured on individual elements within the test array. Total form shear was then determined by summing the drag on all elements within the array. Total shear was then determined by summing particle shear and form shear.

Element densities were 1, 4, and 9 elements per 0.145 m^2. Flow rates were 0.0045 $m^3 \cdot s^{-1}$ and 0.0105 $m^3 \cdot s^{-1}$. This combination resulted in sixteen test scenarios and a range of roughness density from 0.0025 to 0.0912. The observed partition reaches a value of 0.1-0.2 at roughness densities in the range of 0.03 to 0.09.

Shear stress partitioning theories of Raupach (1992) and Wooding et al. (1973) were evaluated for their effectiveness at predicting the ratio of average particle shear to total shear. Both adequately represent the experimentally determined partition. A significant advantage of Raupach's (1992) theory is that it is free of adjustable constants. Future work is needed to investigate a wider range of test scenarios and to link the results from idealized shapes to actual vegetal elements.

CHAPTER 4
SUMMARY AND CONCLUSIONS

The primary focus of research activities is an experimental evaluation of the concept of shear stress partitioning. Water movement across a rough surface exerts a shear force on the surface. Part of the total force is exerted on the large-scale surface roughness (form shear) and the remainder is on the soil particles (particle shear). The significance for erosion prediction is that it is the fraction acting on the soil particles that is responsible for particle detachment. This concept is applied to idealized vegetal elements for overland flow. Vegetation is widely used at construction sites to stabilize earth (hill) slopes and protect against soil erosion. Several objectives were achieved through this research.

Methodology was developed for measuring the shear partition for overland flow. This consisted of the design and construction of laboratory scale instrumentation to measure the individual components of the partition. Unique instrumentation systems were developed to measure both the drag forces on individual rigid elements in overland flow, as well as detailed measurements of particle shear.

The instrumentation to measure drag force consists of a load cell in line with a low friction linear slide. A threaded rod is rigidly connected to the slide and the element is threaded onto the free end of the rod. Drag force on the element causes linear movement in the slide, resulting in a tensile force for the load cell. The force was measured as voltage from the load cell.

The instrumentation to developed to measure particle shear consists of a unique laboratory flume combined with hot-film anemometry. The designed and constructed flume consists of a movable test section floor with a single hot-film sensor mounted in the center. The movable floor is connected to computer driven, linear motion guide rails. This system allows precise movement in the X and Y direction such that the sensor can be placed at any location within a 0.28 m by 0.28 m measurement area. A flush-mounted hot-film sensor and constant temperature thermal anemometer were used to measure high-frequency fluctuations in shear stress. This combination of instrumentation systems is capable of measuring detailed spatial and temporal variations in shear stress.

To determine the shear partition for idealized vegetation, three element densities were studied: one, four and nine elements per 0.145 m^2. Four idealized shapes were used to represent geometric characteristics of vegetation: cylinders, rectangles, trapezoids with large base at bottom, and trapezoids with small base at bottom. Flow rates were 0.0045 and 0.0105 m^3s^{-1}, resulting in a range of flow depths from 0.022 m to 0.058 m, and average flow velocities from 0.39 to 0.78 $m\cdot s^{-1}$. These densities correspond to depth/spacing ratios of 0.039 to 0.20. For each test scenario (16 total), a time series of particle shear was measured at between 32 and 41 locations (dependent on element density). Drag force was measured on all elements within the test array. From these measurements, total form shear and average particle shear were determined. Total shear was the sum of the form and particle shear. Particle shear ranged from 13 to 89% of the total shear. This range indicates the importance of partitioning in understanding detachment processes.

Two shear partitioning theories were evaluated (Raupach, 1992 and Wooding *et al.*, 1973). Both were originally developed for wind erosion and modifications were made to account for overland flow. In addition to measuring the partition, a separate experiment was conducted to determine the dimensionless drag coefficient for each of the idealized shapes. The theory of Raupach (1992) is dependent on this coefficient. In the range of flow conditions investigated, average drag coefficients for non-submerged cylinders, rectangles, trapezoids with large base at bottom, and trapezoids with small base at bottom, are 0.8, 1.55, 1.34, and 1.63, respectively. Based on the observed values for the partition, both theories adequately represent the data. A significant advantage of Raupach's theory is that it is free of adjustable parameters.

REFERENCES

1. Abrahams, A. D., A. J. Parsons, and S. H. Luk. 1986. "Resistance to overland flow on desert hillslopes". J. Hydrology. 88:343-363.

2. Abrahams, A. D. and A. J. Parsons. 1991. "Resistance to overland flow on desert pavement and its implications for sediment transport modeling." Water Res. Res. 27(8):1827-1836.

3. Alam, A. M. Z. and J. F. Kennedy. 1969. "Friction factors for flow in sand-bed channels." J. Hyd. Div., Proc. ASCE. 95(HY6):1973-1992.

4. Arrick Robotics. P.O. Box 1574. Hurst, Texas. 76053.

5. Arya, S. P. S. 1975. "A drag partition theory for determining the large-scale roughness parameter and wind stress on the Arctic pack ice." J. Geophys. Res. 80(24):3447-3454.

6. Beckwith, T. G., N. L. Buck, and R. D. Marangoni. 1982. Mechanical Measurements, Third Edition. Addison-Wesley Publishing Co. Reading, MA.

7. Benik, S.R., B.N. Wilson, D.D. Biesboer, B. Hansen, and D. Stenlund. 1999. "Performance of erosion control blankets under simulated rainfall." Presented at the 1999 ASAE Annual International Meeting, ASAE Paper 992154, 2950 Niles Road, St. Joseph, MI 49085-9659.

8. Bokaian, A. and F. Geoola. 1984. "Wake-induced galloping of two interfering circular cylinders." J. Fluid Mech. 146:383-415.

9. Braas Company. 7970 Wallace Road, Eden Prairie, MN, 55344.

10. Bruun, H. H. 1995. Hot-Wire Anemometry: Principles and Signal Analysis. Oxford University Press, Oxford.

11. Chen, C. 1976. "Flow resistance in broad shallow grassed channels." J. Hyd. Div., Proc. ASCE. 102(HY3):307-322.

12. Data Translation. 2000. SCOPE Version 2.0. 100 Locke Drive, Marlboro, MA 01752-1192.

13. Dillaha, T. A., R. B. Reneau, S. Mostaghimi, and D. Lee. 1989. "Vegetative filter strips for agricultural nonpoint source pollution control." Trans. ASAE. 32(2):513-519.

14. Einstein, H. A. And R. B. Banks. 1950. "Fluid resistance of composite roughness." Trans. Amer. Geophys. Union. 31(4):603-610.

15. Engelund, F. 1966. "Hydraulic resistance of alluvial streams." J. Hyd. Div., Proc. ASCE. 92(HY2):315-326.

16. Foster, G. R. 1982. "Modeling the Erosion Process." IN: Haan, C. T. (ed). Hydrologic Modeling of Small Watersheds. American Society of Agricultural Engineers. St. Joseph, MI.

17. Foster, G. R., C. B. Johnson, and W. C. Moldenhauer. 1982. "Hydraulics of failure of unanchored cornstalk and wheat straw mulches for erosion control." Trans. ASAE. 63:940-947.

18. Garcia, M. H., D. M. Admiraal, J. Rodriguez, and F. Lopez. 1998. "Navigation-induced bed shear stresses: Laboratory measurements, data analysis, and application." Civil Eng. Studies, Hydraul. Eng. Series No. 56.

19. Garde, R. J. and K. G. Ranga Raju. 1985. "Mechanics of Sediment Transportation and Alluvial Stream Problems." John Wiley & Sons, New York.

20. Gharabaghi, B., W. T. Dickinson, and R. Rudra. 2000a. Evaluating rolled erosion control product performance in channel applications. Erosion Control. Jan.Feb. 26-33.

21. Gharabaghi, B., H.R. Whiteley, R. P. Rudra, and W.T. Dickinson. 2000b. "Improving removal efficiency of vegetative filter strips." ASAE Paper No. 002083. St. Joseph, MI: ASAE

22. Ghebreiyessus, Y. T., C. J. Gantzer, E. E. Alberts, and R. W. Lentz. 1994. "Soil erosion by concentrated flow: shear stress and bulk density." Trans. ASAE. 37(6):1791-1797.

23. Golden Software. 1993. SURFER 5.0. Golden Software, Inc.

24. Govers, G. 1990. "Empirical relationships for the transport capacity of overland flow." IAHS Publ. No. 189. 45-63.

25. Govers, G. 1987. "Initiation of motion in overland flow." Sedimentology. 34:1157-1164.

26. Govers, G. And G. Rauws. 1986. "Transporting capacity of overland flow on plane and on irregular beds." Earth Surf. Proc. and Landforms. 11:515-524.

27. Gray, D. H. and R. B. Sotir. 1996. Biotechnical and Soil Bioengineering Slope Stabilization: A Practical Guide for Erosion Control. John Wiley & Sons, Inc. New York.

28. Griffiths, G. A. 1989. "Form resistance in gravel channels with mobile beds." J. Hydraul. Engin. 115(3):340-355.

29. Haan, C. T., B. J. Barfield, and J. C. Hayes. 1994. <u>Design Hydrology and Sedimentology for Small Catchments.</u> Academic Press. San Diego.

30. Hayes, J.C., B.J. Barfield, and R.I. Barnhisel. 1979. "Evaluation of Grass Characteristics Related to Sediment Filtration." <u>ASAE</u> Paper No. 78-2513. St. Joseph. MI, 49085.

31. Jadhav, R.S. and S. G. Buchberger. 1995. "Effects of vegetation on flow through free water surface wetlands." <u>Ecological Engineering</u>. 5:481-496.

32. Kao, D. T. Y. and B. J. Barfield. 1978. "Prediction of Flow Hydraulics for Vegetated Channels". <u>Trans. ASAE</u>. 489-494.

33. Kouwen, N. And R. Li. 1980. "Biomechanics of vegetative channel linings<u>." J. Hydraulics Div. Proc. ASCE</u>. HY6:1085-1103.

34. Kouwen, N. and T. E. Unny. 1973. "Flexible roughness in open channels." <u>J. Hydraulics Div. Proc. ASCE</u>. 99(HY5):713-728.

35. Kramer, L. A. and L. D. Meyer. 1969. "Small amounts of surface mulch reduce soil erosion and runoff velocity." <u>Trans. ASAE</u>. 50:638-645.

36. Lane, L. J. and M. A. Nearing. 1989. USDA – Water Erosion Prediction Project: Hillslope Profile Model Documentation. NSERL Report No. 2. <u>USDA-ARS National Soil Erosion Research Laboratory</u>. West Lafayette, Indiana 47907.

37. Lavelle, J. W. And H. O. Mofjeld. 1987. "Do critical stresses for incipient motion and erosion really exist?" <u>J. Hyd. Eng</u>. 113(3):370-385.

38. Li, M. Z. 1994. "Direct skin friction measurements and stress partitioning over movable sand ripples." J. Geophys. Res. 99(C1):791-799.

39. Li, R. and H. W. Shen, 1973. "Effect of tall vegetation on flow and sediment." J. Hyd. Div., Proc. ASCE. 99(HY5):793-814.

40. Lopez, F., C. Dunn, and M. Garcia. 1995. "Turbulent open-channel flow through emergent simulated vegetation." IN: Water Resources Engineering Volume I ed. by W.H. Espey, Jr and P.G. Combs. ASCE. New York, NY.

41. Magleby, R., C. Sandretto, W. Crosswhite, and C. T. Osborn. 1996. "Soil Erosion and Conservation in the United States: an overview." USDA ERS, Agriculture Information Bulletin No. 718.

42. Marshall, J. K. 1971. "Drag measurements in roughness arrays of varying density and distribution. Agricultural Meteorology." 8:269-292.

43. Morsi, S. A. 1972. An investigation of particle trajectories in two-phase flow systems. J. Fluid Mech. 55(2):193-208.

44. Nepf, H. M. 1999. Drag, turbulence, and diffusion in flow through emergent vegetation. Water Resources Research. 35(2):479-489.

45. Palmer, V.J. 1945. A method for designing vegetated waterways. Ag. Eng. 26(12):516-520.

46. Petryk, S. 1969. Drag on cylinders in open channel flow. Ph.D. Dissertation. Colorado State University, at Fort Collins, Colorado.

47. Petryk, S. and G. Bosmajian III. 1975. Analysis of flow through vegetation. J. Hyd. Div., Proc. ASCE. 101(HY7):871-884.

48. Preston, J. H. 1945. The Determination of Turbulent Skin Friction by means of Pitot Tubes. J. R. Aeronaut. Soc. 58(114):109-121.

49. Prosser, I. P., W. E. Dietrich, and J. Stevenson. 1995. Flow resistance and sediment transport by concentrated overland flow in a grassland valley. Geomorphology. 13:71-86.

50. Raupach, M. R. 1992. Drag and drag partition on rough surfaces. Boundary-Layer Meteorology. 60(4):375-395.

51. *Raupach, M. R., D. A. Gillette, and J. F. Leys. 1993. The effect of roughness elements on wind erosion threshold. J. Geophys. Res. 98(D2):3023-3029.

52. Rauws, G. 1988. Laboratory experiments on resistance to overland flow due to composite roughness. J. Hydrology. 103:37-52.

53. Reda, D. C. and J. J. Muratore Jr. 1994. Measurement of surface shear stress vectors using liquid crystal coatings. AIAA Journal. 32(8):1576-1582.

54. Richardson, E. V. and R. S. McQuivey. 1968. Measurements of Turbulence in Water. J. Hyd. Div., Proc. ASCE. 94(HY2):411-430.

55. Robinson, K. M. 1989. Hydraulic Stresses on an Overfall Boundary. Trans. ASAE. 32(4).

56. Savat, J. 1980. Resistance to flow in rough supercritical sheet flow. Earth Surf. Proc. 5:103-122.

57. Schlichting, H. 1936. Experimental investigation of the problem of surface roughness. NACA Technical Memorandum No. 823. 7(1).

58. Stockton, P. H. and D. A. Gillette. 1990. Field measurement of the sheltering effect of vegetation on erodible land surfaces. Land Degradation and Rehab. 2:77-85.

59. Strawberry Tree, Inc. 1993. Strawberry Tree Data Acquisition. Sunnyvale, CA.

60. Streeter, V. L. and E. B. Wylie. 1985. Fluid Mechanics, eighth edition. McGraw-Hill Publishing Co. New York.

61. Tanner, L. H. 1979. Skin friction measurement by viscosity balance in air and water flows. J. Physics E: Scientific Instrumentation. 12:610-619.

62. Task Committee on Preparation of Sedimentation Manual Committee on Sedimentation. 1966. Sediment transportation mechanics: initiation of motion. J. Hyd. Div. 92(HY2):291-314.

63. Temple, D. M. 1982. Flow retardance of submerged grass channel linings. Trans. ASAE. 63:1300-1303.

64. Thompson, G. T. And J. A. Roberson. 1976. A theory of flow resistance for vegetated channels. Trans. ASAE. 19(2):288-293.

65. Tollner, E. W., B. J. Barfield, C. T. Haan, and T. Y. Kao. 1976. Suspended Sediment Filtration Capacity of Simulated Vegetation. Trans. ASAE. 19:678-682.

66. Tollner, E. W., B. J. Barfield, and J. C. Hayes. 1982. Sedimentology of Erect vegetal filters. J. Hyd. Div., Proc. ASCE. 108(HY12):1518-1531.

67. TSI Inc. Thermal Systems Incorporated. P.O. Box 64204, St. Paul, MN 55164.

68. USDA. 1999. Construction site soil erosion and sediment control factsheet.

69. Vakili, A. D., and J. M. Wu. March 1986. Development of a New Instrument for Direct Skin Friction Measurement. Final Report for NASA, Grant NAG 1-303.

70. van Rijn, L. C. 1984. Sediment transport, Part III: Bed forms and alluvial roughness. J. Hydraul. Eng. 110(12):1733-1754.

71. Wilson, B. N. 1993. Development of a fundamentally based detachment model. Trans. ASAE. 36(4):1105-1114.

72. Wolfe, S. A. and W. G. Nickling. 1993. The protective role of sparse vegetation in wind erosion. Progress in Physical Geography. 17(1):50-68.

73. Wolfe, S. A. And W. G. Nickling. 1996. Shear stress partitioning in sparsely vegetated desert canopies. Earth Surf. Proc. and Landforms. 21:607-619.

74. Wooding, R. A., E. F. Bradley, and J. K. Marshall. 1973. Drag due to regular arrays of roughness elements of varying geometry. Boundary-Layer Meteorology. 5:285-308.

75. Wyatt, V. E. And W. G. Nickling. 1997. Drag and shear stress partitioning in sparse desert creosote communities. Can. J. Earth Sci. 34:1486-1498.

APPENDIX A

SHEAR STRESS CONTOURS FOR DIFFERENT TEST SCENARIOS

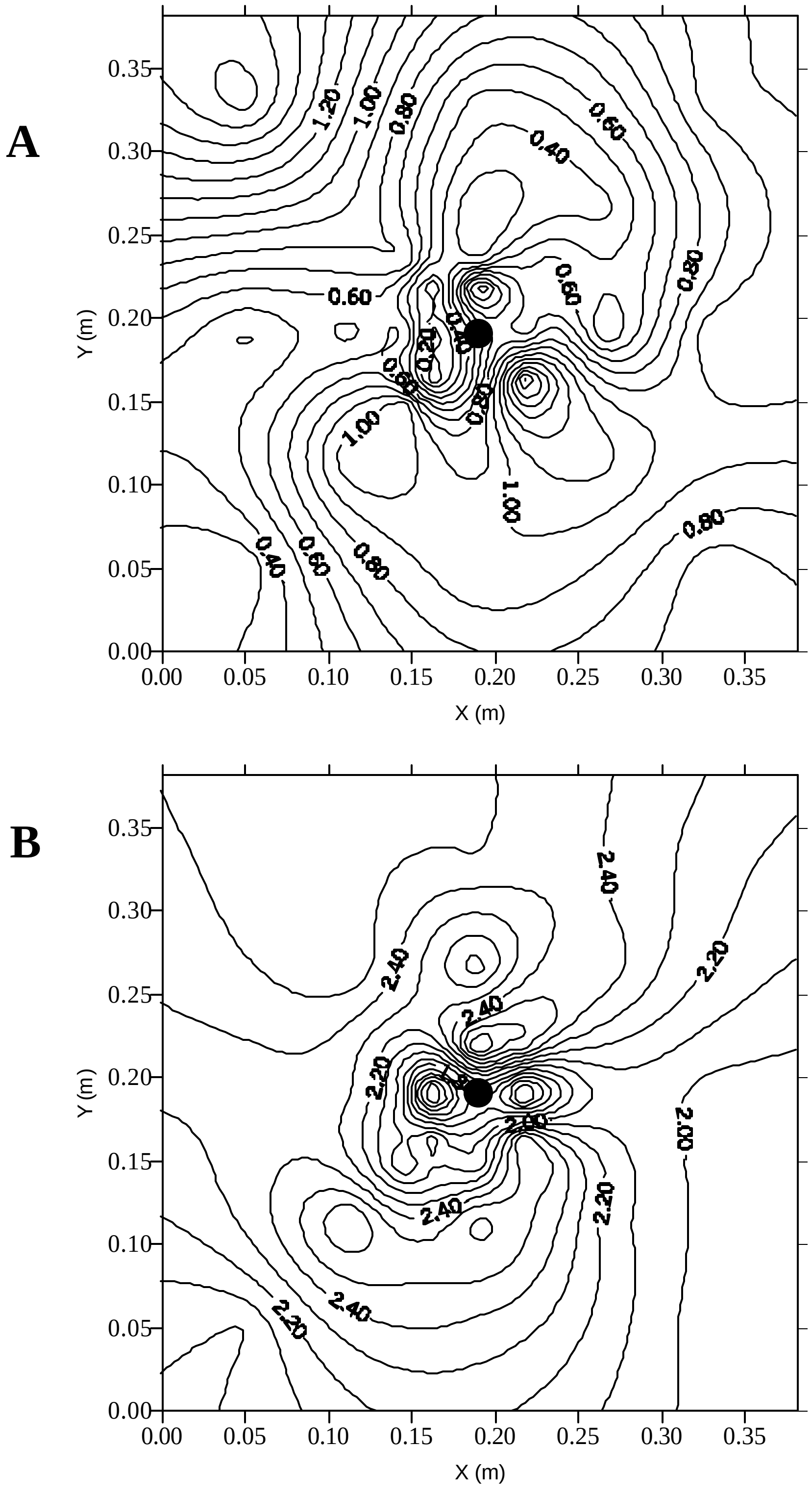

Figure A.1. Shear Stress Contours. A) Test Scenarios C1A and B) Test Scenario C1B

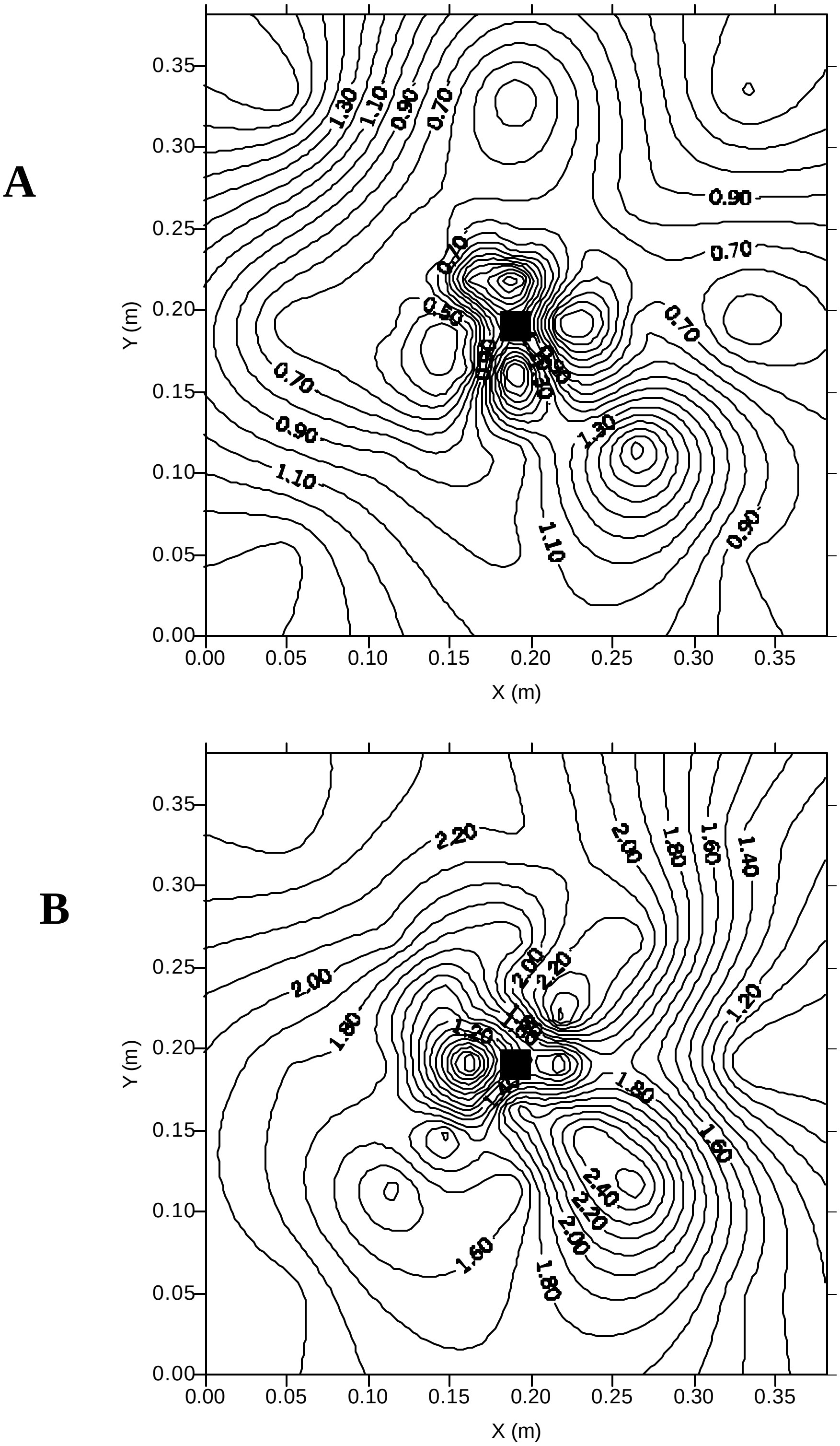

Figure A.2. Shear Stress Contours. A) Test Scenarios R1A and B) Test Scenario R1B.

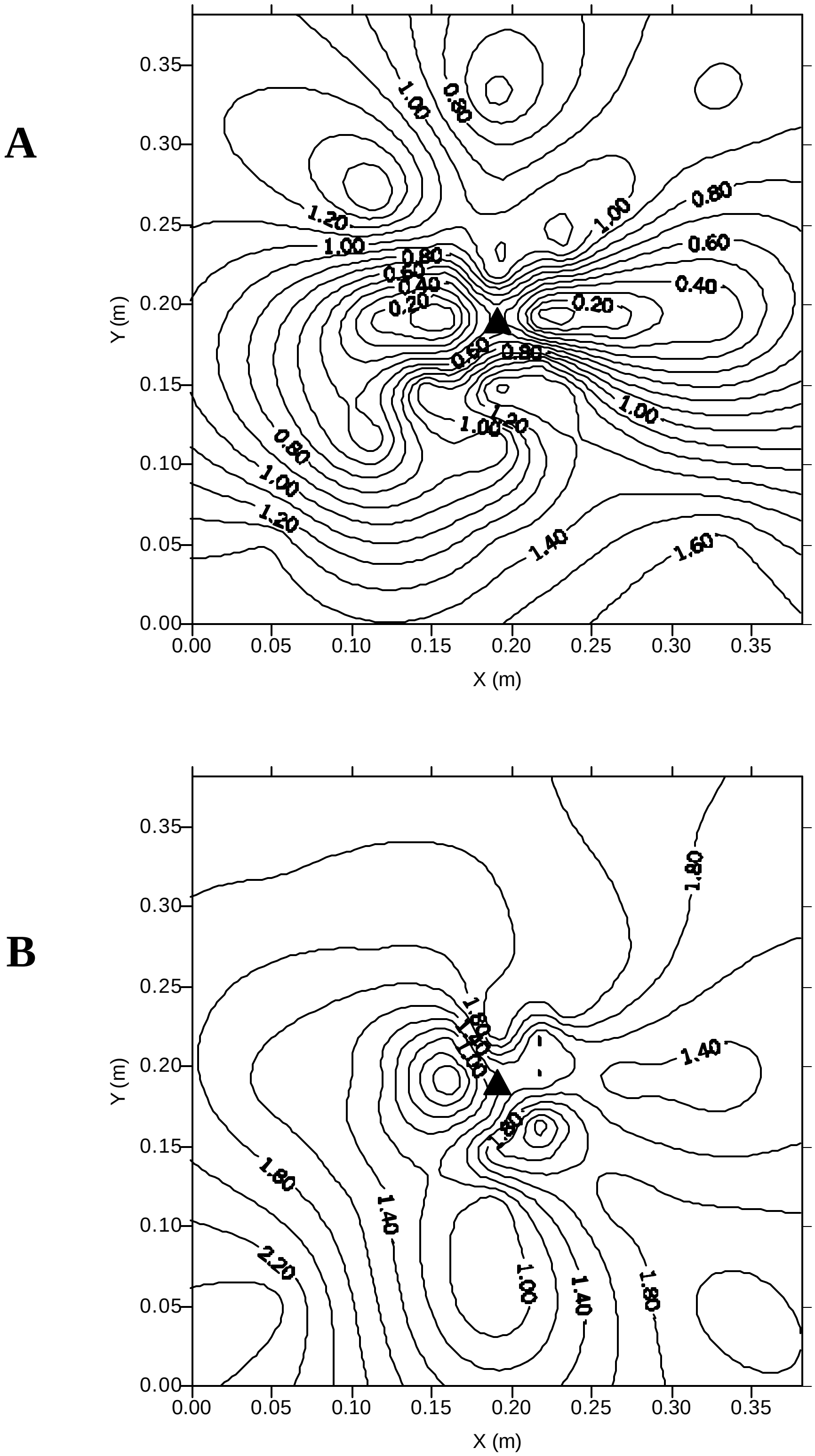

Figure A.3. Shear Stress Contours. A) Test Scenarios TL1A and B) Test Scenario TL1B.

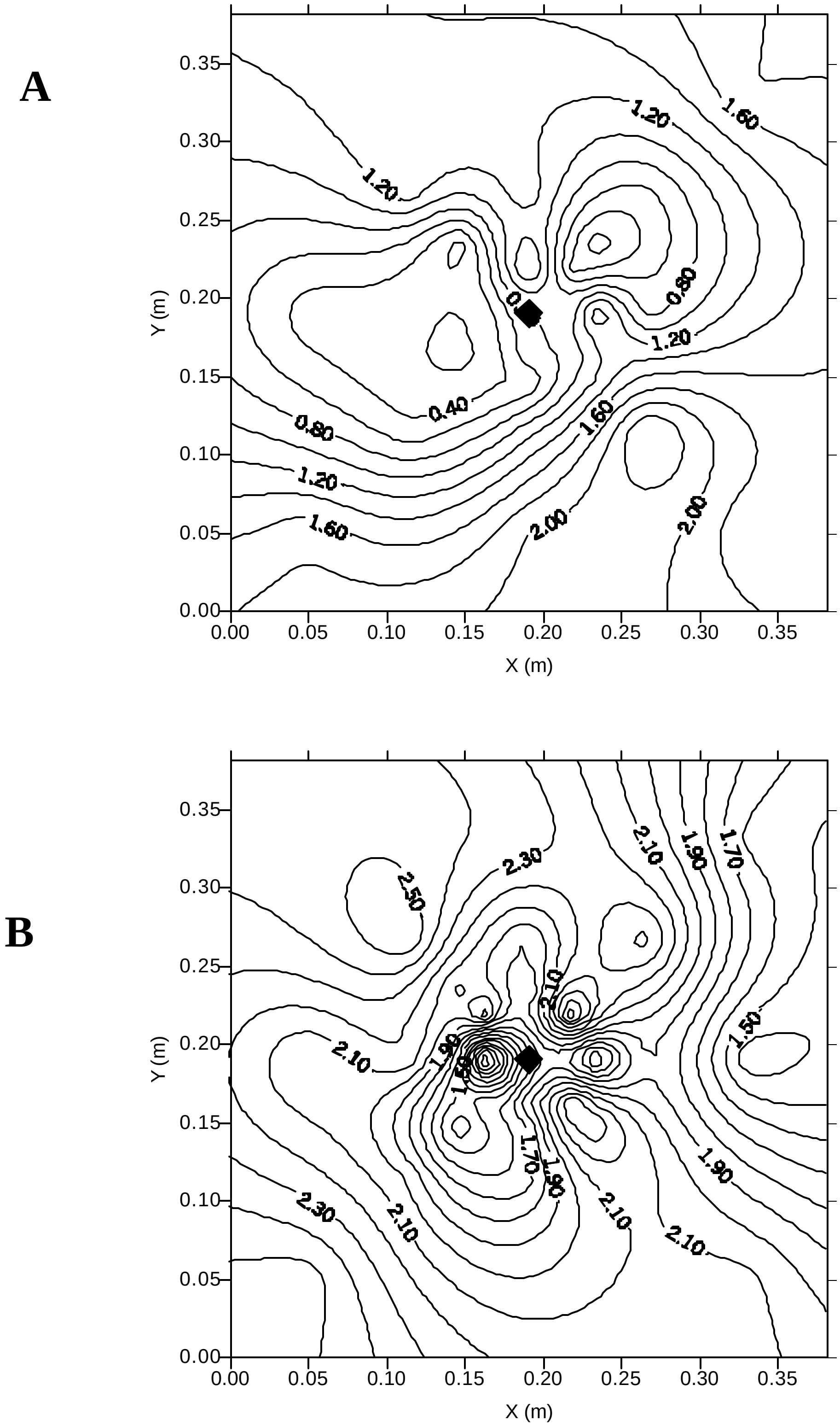

Figure A.4. Shear Stress Contours. A) Test Scenarios TS1A and B) Test Scenario TS1B.

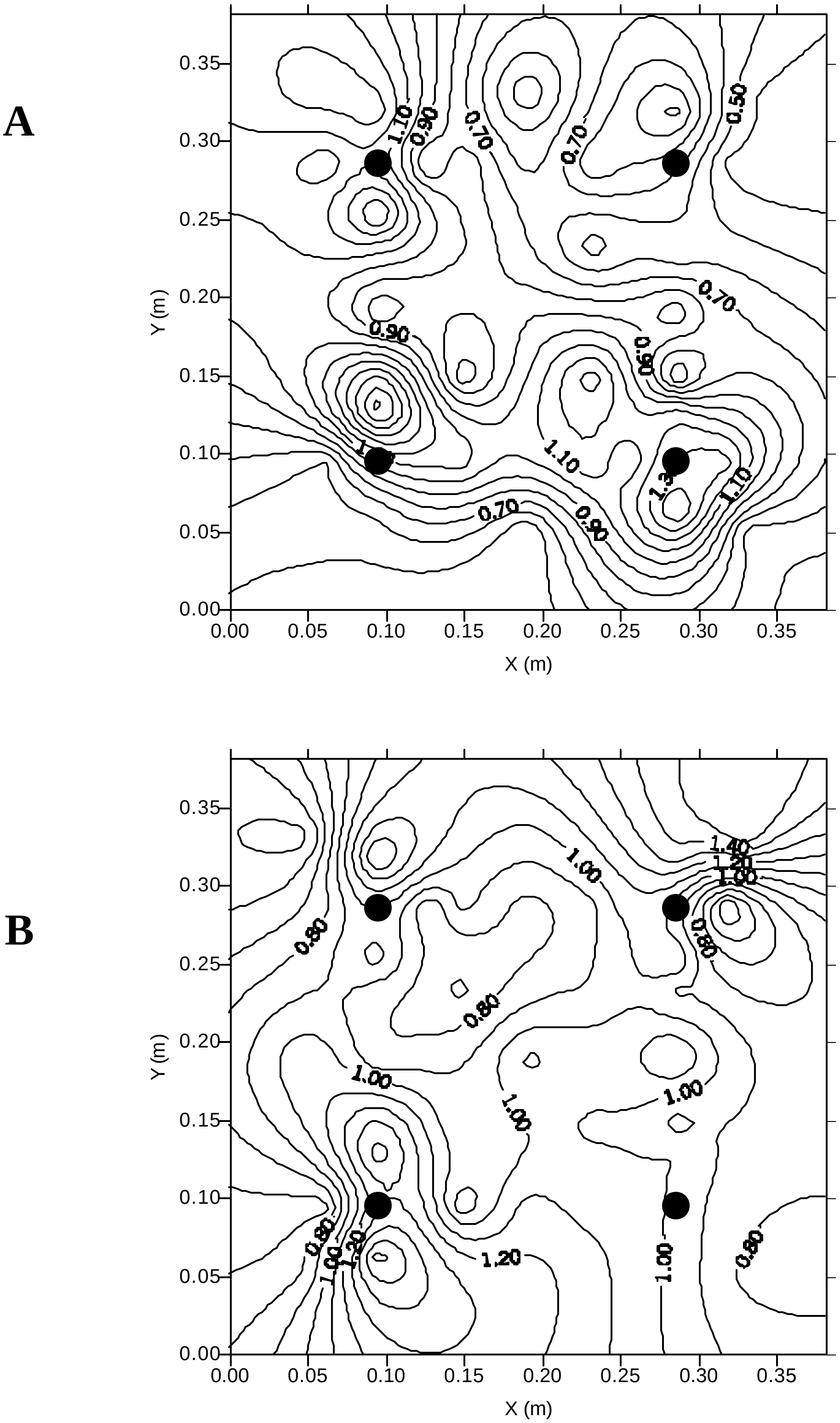

Figure A.5. Shear Stress Contours. A) Test Scenarios C4A and B) Test Scenario C4B.

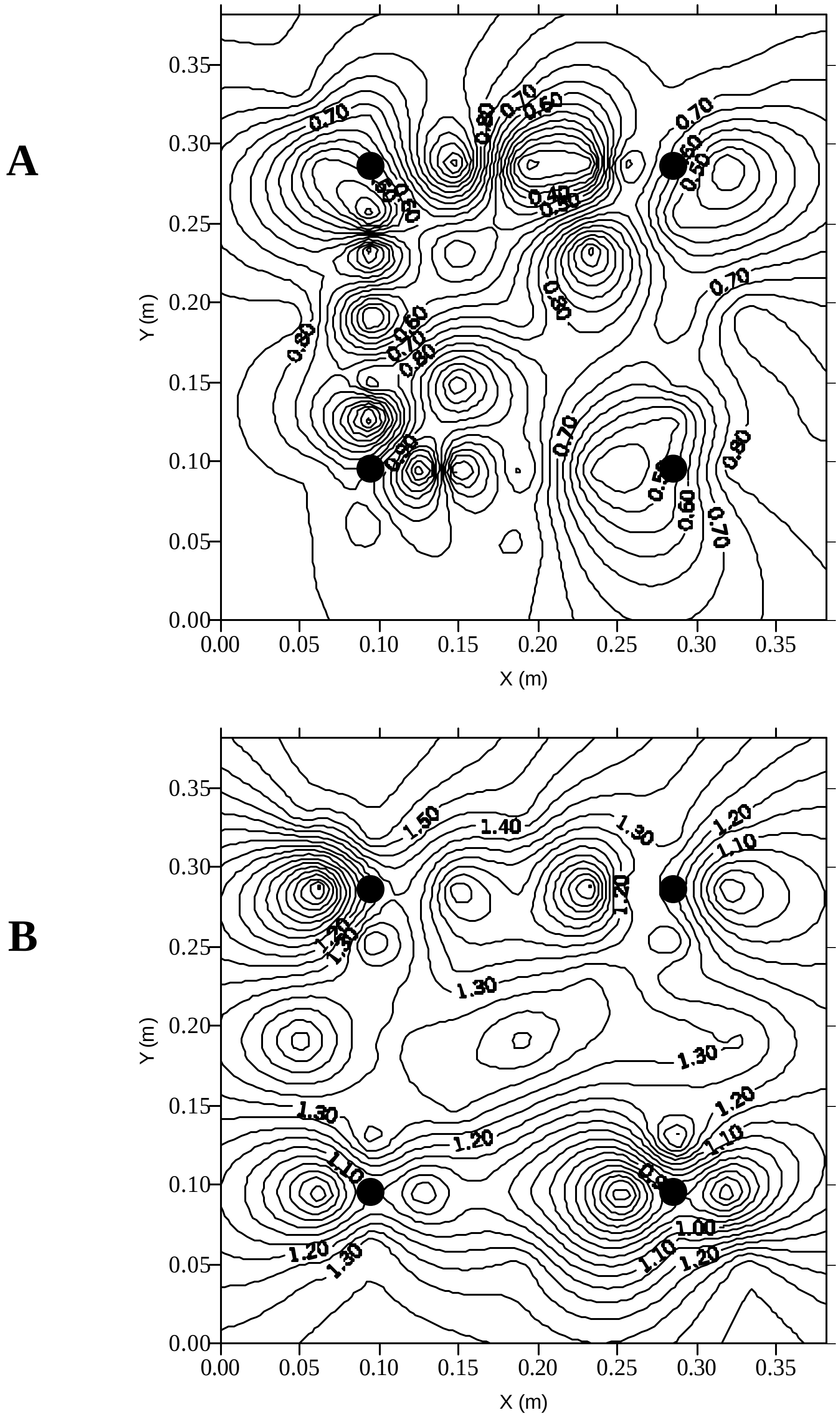

Figure A.6. Shear Stress Contours. A) Test Scenarios SC4A and B) Test Scenario SC4B.

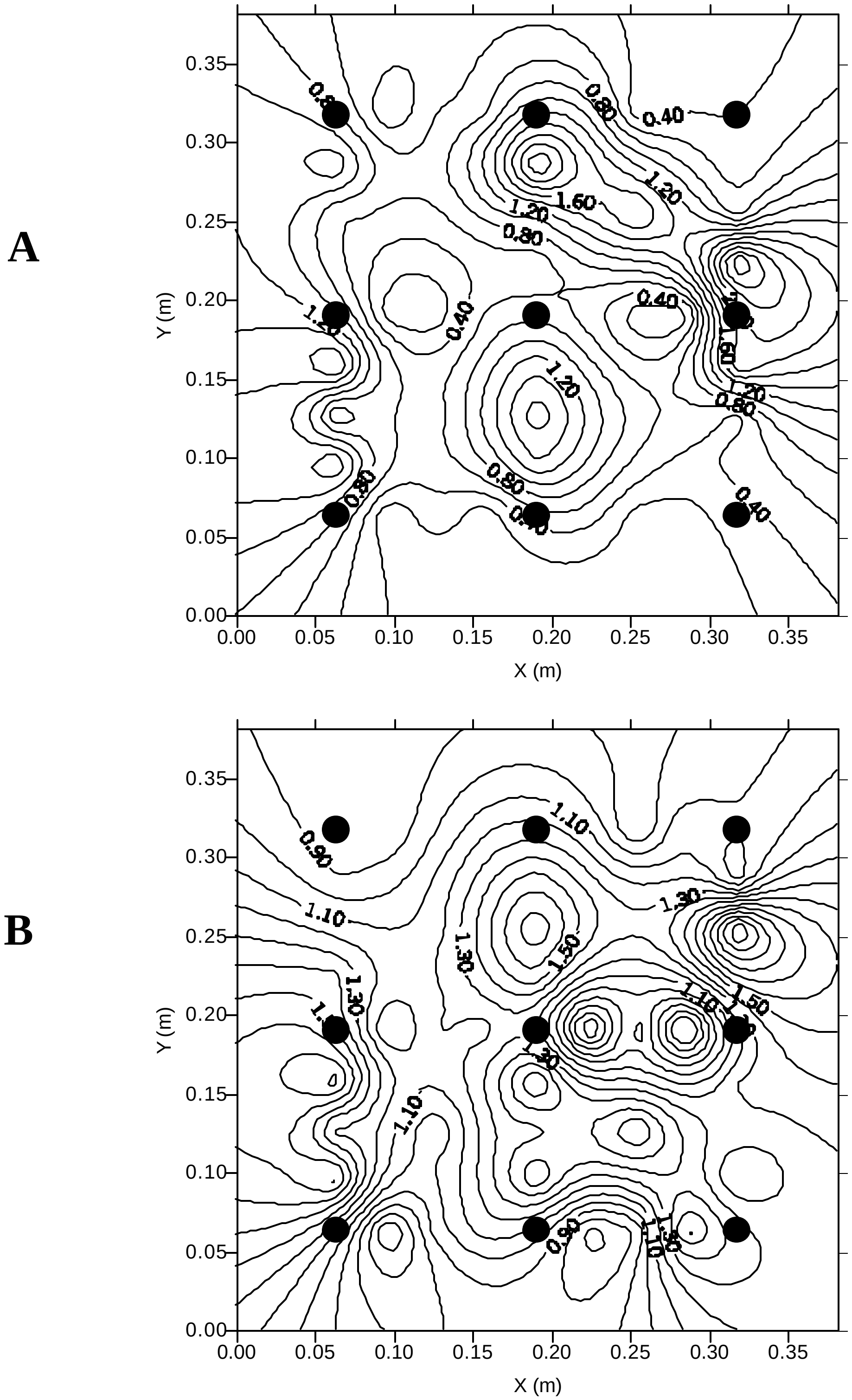

Figure A.7. Shear Stress Contours. A) Test Scenarios C9A and B) Test Scenario C9B.

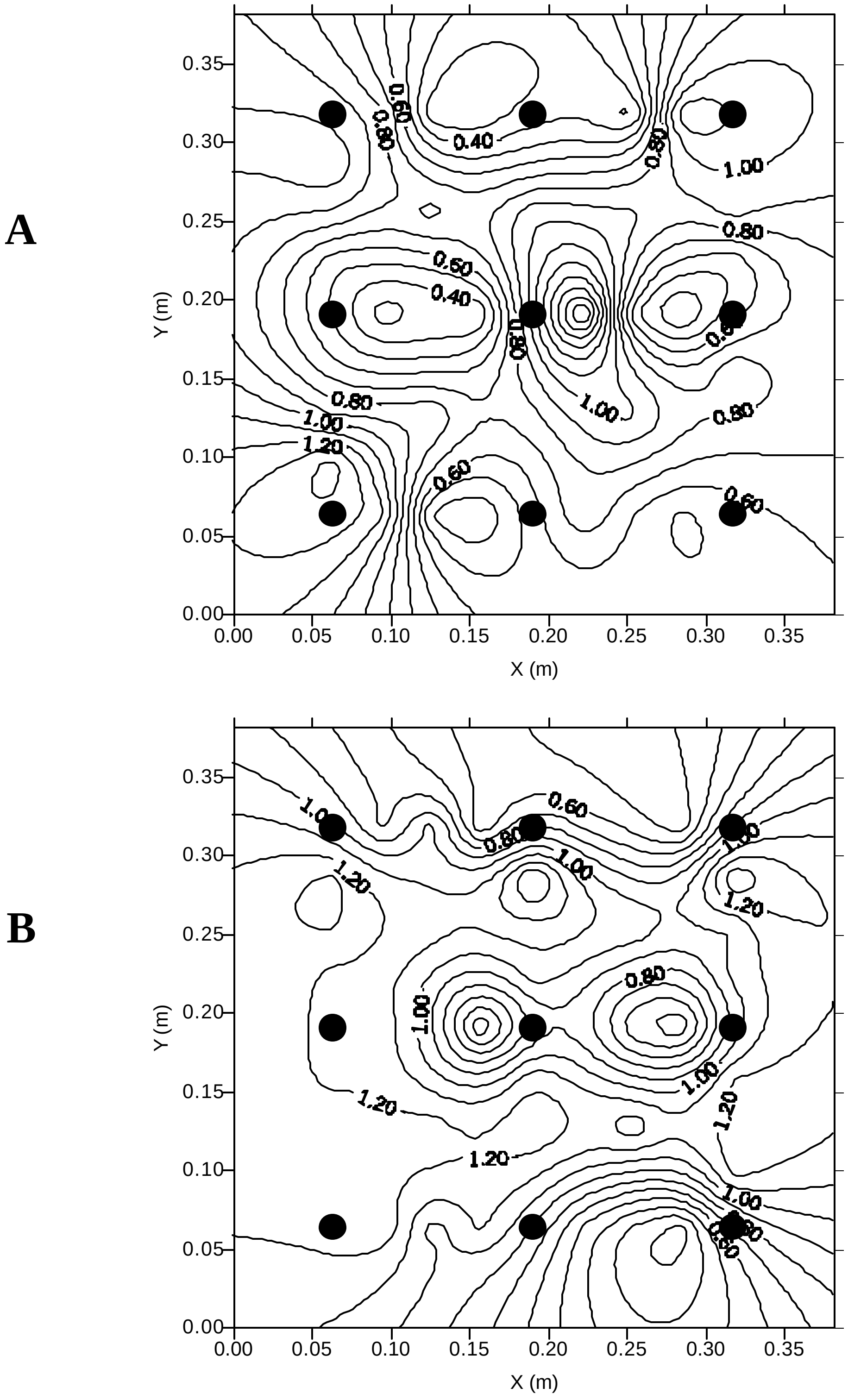

Figure A.8. Shear Stress Contours. A) Test Scenarios SC9A and B) Test Scenario SC9B.